

Microseismicity appears to outline highly coupled regions on the Central Chile megathrust

C. Sippl¹, M. Moreno², R. Benavente^{3,4}

¹Institute of Geophysics, Czech Academy of Sciences, Prague, Czech Republic

²Departamento de Geofísica, Universidad de Concepción, Concepción, Chile

³Departamento de Ingeniería Civil, Universidad Católica de la Santísima Concepción, Concepción, Chile

⁴National Research Center for Integrated Natural Disaster Management (CIGIDEN), Santiago, Chile

Key Points:

- Plate interface seismicity in Central Chile outlines three half-ellipses
- These seismicity patterns may define the outline of highly coupled regions
- GPS data is shown to be compatible with the existence of such features

Corresponding author: Christian Sippl, sippl@ig.cas.cz

This article has been accepted for publication and undergone full peer review but has not been through the copyediting, typesetting, pagination and proofreading process, which may lead to differences between this version and the [Version of Record](#). Please cite this article as [doi: 10.1029/2021JB022252](https://doi.org/10.1029/2021JB022252).

This article is protected by copyright. All rights reserved.

Abstract

We compiled a novel microseismicity catalog for the Central Chile megathrust (29–35°S), comprising 8750 earthquakes between 04/2014 and 12/2018. These events describe a pattern of three trenchward open half-ellipses, consisting of a continuous, coast-parallel seismicity band at 30–45 km depth, and narrow elongated seismicity clusters that protrude to the shallow megathrust and separate largely aseismic regions along strike. To test whether these shapes could outline highly coupled regions (“asperities”) on the megathrust, we invert GPS displacement data for interplate locking. The best-fit locking model does not show good correspondence to seismicity, possibly due to lacking resolution. When we prescribe high locking inside the half-ellipses, however, we obtain models with similar data fits that are preferred according to the Bayesian Information Criterion (BIC). We thus propose that seismicity on the Central Chile megathrust may outline three adjacent highly coupled regions, two of them located between the rupture areas of the 2010 Maule and the 2015 Illapel earthquakes, a segment of the Chilean margin that may be in a late interseismic stage of the seismic cycle.

Plain Language Summary

The largest earthquakes commonly occur along plate boundary faults, where one tectonic plate slides under another. How big such earthquakes can get depends on the properties of the fault, which often vary along its length. By identifying and locating thousands of small earthquakes on the plate boundary fault in Central Chile, we have found a curious pattern: these earthquakes describe three half-ellipses, inside which only few earthquakes occur. We believe that this pattern can show us regions of the plate boundary fault where stress is accumulated to be one day released in a large earthquake. Aseismic patches are the ones that accumulate stress and are thus being “loaded” for a larger earthquake, whereas those that constantly produce small earthquakes are only storing part of the energy that is provided by the convergence of plates. We think that our results provide additional information on the state of the plate boundary fault in Central Chile.

1 Introduction

Subduction zone megathrusts are segmented in the downdip and along-strike direction. Downdip segmentation occurs primarily due to differences in temperature, rigidity and possibly pore fluid pressure, which leads to an unstable (velocity-weakening) and thus seismogenic central segment framed by conditionally stable or stable segments above and below (Lay & Kanamori, 1981; Oleskevich et al., 1999; Lay et al., 2012). Large megathrust earthquakes commonly originate on the central, unstable part of the plate interface, but occasionally also break the conditionally stable zone above all the way to the trench (like the 2011 M_w 9.0 Tohoku earthquake: Fujiwara et al., 2011; Ide et al., 2011). The seismogenic central segment is laterally heterogeneous, and consists of highly coupled areas (“asperities”) that accumulate stress during the interseismic period, and partially coupled areas that release part of the plate convergence as aseismic slip (Perfettini et al., 2010). The distribution of interseismic locking (we attempt to use the terms locking and coupling as suggested in Wang and Dixon (2004)) on the plate interface can be constrained from GPS data (Pacheco et al., 1993), and there is a general correspondence between imaged highly locked areas and slip distributions of large earthquakes (e.g. Chlieh et al., 2008; Moreno et al., 2010; Loveless & Meade, 2011), although asperities *sensu stricto*, with full mechanical coupling, have been found to be significantly smaller than earthquake ruptures (Bürgmann et al., 2005).

The origin of megathrust asperities, and whether they are long-lived or transient, is currently not fully understood. The occurrence of regions of higher interseismic coupling has been ascribed to topographic features on the incoming plate (Sykes, 1971; Cloos,

1992), plate interface curvature (Bletery et al., 2016), variable pore fluid pressure (e.g. Moreno et al., 2014), or combinations of these factors. Highly coupled areas on the megathrust appear to be associated with anomalously low levels of background seismicity, as noted by Kanamori (1981) and confirmed by numerous studies since. Weakly coupled areas that separate asperities can act as barriers to large earthquake ruptures, and the width, coupling ratio and stress state of such barriers determines whether a large earthquake is capable of rupturing across it (e.g. Corbi et al., 2017).

In this study, we combine the analysis of seismicity patterns and GPS data for the megathrust of Central Chile. A high-resolution earthquake catalog containing 8,750 events on the Central Chile plate interface shows geometries resembling half-ellipses surrounding aseismic regions, similar to recent observations preceding the 2014 Iquique earthquake in Northern Chile (Schurr et al., 2020). To check whether the seismicity geometries we observe could be indicative of areas of elevated interplate coupling on the megathrust, we check whether GPS data are compatible with such a distribution of highly coupled patches.

2 Study region

The Central Chilean margin is created by the ENE-ward subduction of the Nazca Plate beneath the South American Plate with a speed of approx. 66 mm/yr (e.g. Angermann et al., 1999). The margin is classified as accretionary (von Huene & Scholl, 1991) and features the subduction of two notable seafloor features, the Juan Fernandez Ridge near 32.5°S and the Challenger Fracture Zone near 30°S (Contreras-Reyes & Carrizo, 2011, Figure 1). Intraslab seismicity (e.g. Anderson et al., 2007; Marot et al., 2013) shows that the Nazca slab transitions from a flat slab configuration (the Pampean flat slab, see e.g. Ramos & Folguera, 2009, Figure 1) to a normally subducting geometry at 32-33°S (Figure 2). A causal connection between the subduction of the Juan Fernandez Ridge and the formation of the Pampean flat slab has been suggested (Ramos et al., 2002).

Whereas crustal seismicity in most of the Central Chilean forearc is relatively sparse, with most upper plate seismicity confined to the regions adjacent to the Western Cordillera (Barrientos et al., 2004), the Central Chile megathrust has experienced many $M \geq 8$ earthquakes over past centuries (Figure 3a; Comte & Pardo, 1991; Lomnitz, 2004; S. Ruiz & Madariaga, 2018). Since the 1730 earthquake that ruptured the entire study area (Carvajal et al., 2017), megathrust earthquakes in Central Chile have featured limited size ($M 8-8.5$) and relatively stable recurrence in space and time (S. Ruiz & Madariaga, 2018). The 2015 M_w 8.3 Illapel earthquake was the most recent event in the north of the study area, and was preceded by similar-sized events in 1880 and 1943 (Figure 3a). The northern and southern termination of their rupture areas coincide with subducting seafloor features on the incoming Nazca plate, the Challenger Fracture Zone (CFZ) and Juan Fernandez Ridge (JFR) (Tilman et al., 2016; Lange et al., 2016), consistent with the suggestion that such seafloor features can be efficient rupture barriers along the Chilean margin (e.g. Contreras-Reyes & Carrizo, 2011; Sparkes et al., 2010). Further south, a second series of presumably similar-sized events in 1822, 1906 and 1985 have occurred south of the JFR. The northern termination of the 2010 Maule earthquake (M_w 8.8) rupture at $\sim 34^\circ\text{S}$ (Figure 3b; Moreno et al., 2010; Vigny et al., 2011) marks the end of our study region. It has recently been proposed that the 1985 and 1906 events (and thus likely also the 1822 one) only ruptured the deeper part of the megathrust (S. Ruiz & Madariaga, 2018; Bravo et al., 2019), which would imply that the shallower part of the megathrust in the region between the Illapel and Maule earthquakes (Figure 3b) has been unruptured since 1730. We concede that our knowledge especially about the older $M \geq 8$ earthquakes (1822, 1880) is very limited; we cannot exclude that there were ruptures that affected the shallow part of the plate interface between 1730 and now.

3 Seismicity observations

3.1 Data and Processing

We analyzed raw waveform data from 32 broadband seismic stations in Central Chile ($\sim 29.5\text{--}34.5^\circ\text{S}$) to derive a microseismicity catalog, applying a modified version of the automated earthquake detection and location workflow of Sippl et al. (2013). The main constituents of this workflow are initial triggering using a recursive STA/LTA algorithm (Withers et al., 1998), event association on a traveltimes grid, re-picking of P- and S-phases using higher-level algorithms that operate on narrow time windows (Di Stefano et al., 2006; Diehl et al., 2009), and the stepwise improvement of locations through joint hypocenter determination (e.g. Kissling et al., 1994), relocation in a 2D velocity model and finally double-difference relocation. For a detailed description of the different steps of this workflow, the reader is referred to the Appendix of Sippl et al. (2013).

The data cover the time period from 04/2014 to the end of 2018, and are available from IRIS webservices (networks C, C1, G, IU, WA; see Acknowledgments). In the initial triggering, event association and repicking stages, the 1D velocity model of Lange et al. (2012) was used; for the later relocation steps, we calculated a 2D velocity model (see Figure S2 and description in its caption) from a subset of the analyzed hypocenters using the simul2000 algorithm (Thurber & Eberhart-Phillips, 1999). The final hypocentral relocation was carried out with the double-difference code hypoDD (Waldhauser & Ellsworth, 2000), in which both catalog traveltimes differences (1,227,880 P and 555,781 S) and cross-correlation lagtimes (100,873 P and 34,504 S; only if $CC > 0.7$ and distance between event pairs < 15 km) were used. RMS residuals of phase arrivals were reduced by 26% for catalog traveltimes and 80% for cross-correlation lagtimes during relocation. This procedure yielded a total of 11,788 double-difference relocated earthquakes at depths between 0 and 200 km (Figure 2), with local magnitudes between 1.4 and 7.7. The catalog is available as a supplementary file to this article. Due to significant changes in network geometry during the investigated time period (see Figure 4), it is not meaningful to determine a single completeness magnitude for our catalog. Based on the station distributions, we can assert that the catalog should be more complete at later times (2017/18) compared to earlier times, and in the south of the study region compared to the north.

Since the present study is focused on active processes at the plate interface, we selected only events located at depths < 60 km and west of where the slab surface (from the slab2 model; Hayes et al., 2018) reaches 60 km depth. This leaves a total of 8750 events, which are shown in Figure 3. Relative location uncertainties for these events were determined by bootstrapping and jackknifing tests (Waldhauser & Ellsworth, 2000), in which the robustness of locations relative to the removal of stations (jackknife) and the random perturbation of traveltimes differences (bootstrap) are tested. Results of these tests are shown in Figure S1. Relative location uncertainties are smallest in latitudinal and largest in depth direction, which is to be expected considering the event-station geometry (Figures 2, 4). Standard deviations are 1.07/0.49/1.26 km (jackknife) and 2.39/1.14/4.45 km (bootstrap) in east-west, north-south and vertical direction (Figure S1).

3.2 Results

Since the focus of the present study is the megathrust, we do not further discuss the deeper intraslab earthquakes that depict the transition from a flat to a normally subducting slab (Ramos et al., 2002) across our study region (profiles A-A' and B-B', Figure 2), but focus on depths < 60 km, where the majority of retrieved events is located (8750 of 11931; Figure 3). The profile sections (Figure 2) as well as Figure 5 show that the vast majority of these earthquakes is located within 10 vertical km from the slab surface contour from the slab2 model (Hayes et al., 2018). Focal mechanisms of shallow earthquakes, harvested from the GEOFON and globalCMT databases, show nearly exclusively low-angle thrusting. Taken together, these observations likely imply that a majority of the events shown in Figure 3 occurred on the plate interface (see Discussion Section 6.1).

164 This is supported by earlier higher-resolution local-scale studies (Barrientos et al., 2004;
165 Marot et al., 2013) that concluded that upper plate seismicity in the region is rather scarce.

166 The hypocenters in Figure 3 describe an along-strike continuous band at depths
167 of 30-45 km, located just west of the coastline, which should roughly coincide with the
168 downdip limit of interplate coupling (Chlieh et al., 2004; Béjar-Pizarro et al., 2013). Fur-
169 ther updip, seismicity is confined to elongated active regions which we call “separators”.
170 These extend updip to depths as shallow as \sim 10-15 km and separate larger, aseismic ar-
171 eas on the shallow megathrust in along-strike direction. This leads to the appearance
172 of three half-ellipses, open towards the trench, that are outlined by seismicity (see Fig-
173 ures S4, 3). The northernmost of the three identified half-ellipses corresponds remark-
174 ably well to the extent of slip during the 2015 Mw 8.3 Illapel earthquake (e.g. Tilmann
175 et al., 2016; Melgar et al., 2016; Benavente et al., 2016). Although we only show one of
176 several existing slip models for the Illapel earthquake in Figure 3, this assertion holds
177 for most other models because published models mostly differ in their maximum slip and
178 in whether or not they show rupture to the trench, but they are not very different in terms
179 of along-strike rupture extent. Note that the majority of earthquakes surrounding the
180 Illapel slip area are aftershocks (Figure 4, Section 6.1). The other two half-ellipses are
181 confined to the region between the 2015 Illapel and the 2010 Maule earthquakes, where
182 the megathrust may not have been ruptured since 1730. The region north of the Illapel
183 earthquake shows more widespread seismicity extending to the shallow plate interface
184 (Figure 3b).

185 3.3 Repeating earthquakes

186 The occurrence of repeating earthquakes, low-magnitude events with near-identical
187 waveforms, is considered as a seismological proxy for the presence of aseismic creep (e.g.
188 Uchida & Bürgmann, 2019). Identifying such repeaters can thus provide an additional
189 line of evidence for slow processes independent from geodetic methods. We searched for
190 repeating earthquakes in the catalog of plate interface earthquakes by computing cross-
191 correlations for event pairs whose epicenters were located at a distance of less than 15
192 km from each other, for stations where both events had catalog P-picks. The correlated
193 time windows were 35 seconds long, from 5 seconds before to 30 seconds after the P-pick,
194 which means that they included the S-phase in most cases. The data was bandpass fil-
195 tered to between 1 and 5 Hz before the correlation. We defined a pair of earthquakes as
196 belonging to one “repeater family” if they achieved a cross-correlation coefficient of >0.95
197 at two or more stations (Uchida & Matsuzawa, 2013). In Figure 3, we show repeater fam-
198 ilies with at least three constituent events. We obtained a total of 168 such families, con-
199 taining between 3 and 16 repeating earthquakes, all of which show highly similar mag-
200 nitudes and catalog locations for their constituent events. Obtained repeaters form sev-
201 eral clusters, the most prominent of which is the Vichuquén cluster (Valenzuela-Malebran
202 et al., 2021) at \sim 34.7°S. A high concentration of repeaters is also found in the region
203 of the 2017 Valparaíso earthquake sequence (S. Ruiz et al., 2017), on the deeper part of
204 the plate interface around 30.7°S, and on the northernmost seismicity separator. It is
205 notable that the region of the 2017 Valparaíso sequence became active during the Illapel
206 sequence in 2015 despite its location >100 km from the rupture area. The highly active
207 band of seismicity at 30-45 km depth (except for the aforementioned clusters) shows only
208 very few repeating earthquakes.

209 4 GPS data and unconstrained locking inversion

210 The inversion of GPS data for interseismic locking is the principal means by which
211 the coupling properties of the megathrust are commonly illuminated. In order to check
212 whether locking maps derived from geodetic data show similarities to what we imaged
213 with seismicity, we used a kinematic inversion based on measured GPS velocities to es-
214 timate the degree of coupling on the Central Chilean plate interface. We applied the back-

215 slip modelling approach (Savage, 1983), in which the continuous relative plate motion
216 is accommodated by non-slipping (locked) and aseismically slipping zones on the inter-
217 face. The kinematic fault locking is described as the fraction of plate convergence not
218 accommodated by aseismic slip between great earthquakes. It is calculated by dividing
219 the estimated back-slip rate by the plate convergence rate, which is ~ 66 mm/yr in the
220 study area (Angermann et al., 1999; Kendrick et al., 2003). Thus, the degree of locking
221 ranges from 0 for areas where the entire plate convergence is accommodated by free slip,
222 to 1 for completely non-slipping, i.e. fully locked, patches. As input for the inversion,
223 we used a set of 186 horizontal (north and east components) published GPS vectors (Fig-
224 ure 6a; compiled by Métois et al. (2016); based on Klotz et al. (2001); Brooks et al. (2003);
225 Vigny et al. (2009)) that cover the forearc, arc and even extend into the backarc along
226 the entire along-strike extent of the inversion grid. We transformed these velocities to
227 a stable South American continent reference frame. These data were acquired in the decade
228 before the 2010 Maule earthquake, the last time when Central Chile was completely in
229 the interseismic period and no major overprinting of GPS velocities by postseismic pro-
230 cesses occurred. Since then, the areas of the 2010 Maule earthquake (M_w 8.8) and the
231 2015 Illapel earthquake (M_w 8.3) have ruptured, and their postseismic relaxation pro-
232 cesses contaminate the GPS velocity field to this day. We attempted to use current GPS
233 data recorded contemporaneously with the seismicity, but postseismic contamination in
234 the vicinity of these two earthquake areas prevented us from retrieving reliable locking
235 models. However, we believe that the size and position of asperities, especially in the ar-
236 eas that did not rupture, should not experience significant changes within a decade.

237 We used 3D-spherical viscoelastic finite-element models (FEMs) and built viscoelas-
238 tic Green's Functions (GFs) following the method of Li et al. (2015). The FEMs include
239 topography and bathymetry, as well as a realistic geometry of the slab and continental
240 Moho (Tassara & Echaurren, 2012; Hayes et al., 2012). The model consists of the elas-
241 tic part of the downgoing slab (oceanic plate) and an upper plate unit (see sketch in Fig-
242 ure S6), both sitting on a viscoelastic unit that comprises the asthenosphere as well as
243 the deeper parts of the oceanic lithosphere. We used a Young's modulus of 100, 120 and
244 160 GPa for the continental, elastic oceanic and viscoelastic layers, respectively. The Pois-
245 son's ratio was set to 0.265 for the continental and 0.3 for the elastic oceanic layer, and
246 the thickness of the elastic part of the oceanic plate (T_e) was set to 30 km (e.g. Moreno
247 et al., 2011). Density values of 2,700 and 3,300 kg/m^3 were used for the continental and
248 elastic oceanic layers, respectively.

249 The inversion was performed on the fault nodes located at a depth of less than 70
250 km, yielding a total of 353 nodes (Figure 6a). We estimated the GFs for the downdip
251 and along-strike components using Pylith (Aagaard et al., 2013). At the bottom edge
252 of the fault plane, we constrained the back slip to zero, assuming aseismic slip below the
253 seismogenic zone. Minimum and maximum slip constraints are applied to avoid mod-
254 els with unreasonable slip patterns and to improve the model resolution. Thus, the back-
255 slip rate is constrained to range between 0 and 66 mm/yr, representing freely slipping
256 and fully locked areas, respectively. The smoothing parameter, β , is estimated from the
257 trade-off curve between misfit and slip roughness. The inversion is stabilized by utiliz-
258 ing Laplacian smoothing regularization with observations being weighted according to
259 the reported station measurement error (usually ~ 2 mm/yr). The optimal solution (shown
260 in Figure 6b) is then found by employing a bounded least squares scheme.

261 The best-fitting retrieved locking model is shown in Figure 6. It features a highly
262 locked region in the south, roughly coinciding with the source region of the 2010 Maule
263 earthquake, and a region of overall low locking north of 30.5°S . Between these regions,
264 the overlay with the seismicity (Figure 6b) shows no clear correspondence between the
265 seismicity half-ellipses and highly locked patches, which would be expected if the seis-
266 micity indeed outlined regions of elevated locking. While regions of elevated interplate
267 locking at relatively shallow depth on the megathrust are imaged around where the north-
268 ern and southern half-ellipse are located, the central half-ellipse appears to coincide with
269 rather low locking. There, higher locking values are retrieved where the downdip band

of continuous microseismicity is located (Figure 6b). However, synthetic tests (Figure 7) demonstrate that the resolution of the locking map is limited, especially in the offshore regions; station density and hence resolution are lowest in the region where low locking at shallow depths coincides with the seismicity half-ellipse.

5 Locking inversions constrained by seismicity

As shown in Section 4, the resolution of the GPS inversion does not allow us to clearly state that there is no high locking inside the seismicity patterns we observe. While high locking is mapped into the aseismic regions outlined by seismicity in the case of the northernmost and the southernmost such region, the central aseismic region coincides with low locking in the unconstrained inversion (Figure 6), and higher locking is obtained further downdip, where high seismicity levels prevail. The synthetic checkerboard test (Figure 7) shows us that the GPS data have rather low resolving power offshore, even if we optimistically assume no data noise. The unconstrained inversion thus tells us that a coincidence of seismicity half-ellipses and high interplate coupling is not required to fit the GPS data. Since GPS data currently provide the most direct insight into the locking state of at least the onshore portion of a megathrust, we additionally test whether these data require the absence of such features. If GPS data are incompatible with the proposed highly coupled asperities, one could reasonably rule out their existence.

Locking patterns derived from interseismic geodesy show heterogeneous plate interfaces with anomalies that mostly correlate with coseismic slip distributions (e.g. Chlieh et al., 2008; Moreno et al., 2010; Loveless & Meade, 2016). They can thus identify areas with high slip deficit along the deeper portion of the megathrust, while they usually have limited resolution for its shallower part. Coupling estimates are highly dependent on the amount and distribution of geodetic data, modeling assumptions and inversion technique. Thus, even locking distributions for the same area calculated with similar data can differ significantly (e.g. Moreno et al., 2010; Métois et al., 2012; Chlieh et al., 2011; Schurr et al., 2014). If the seismicity pattern we observe indeed outlines highly coupled asperities, then the seismicity may offer additional and independent information that could be used to improve GPS-based locking inversions. The GPS inversion in Section 4 has not provided strong evidence for a co-location of highly coupled regions and the aseismic areas inside the microseismicity half-ellipses. However, if the seismicity pattern we observe indeed outlines highly coupled asperities, then the seismicity may offer additional and independent information that could be used to improve the GPS-based locking inversions.

In order to check whether the data instead provide evidence against the existence of such a co-location, or whether they can simply not resolve it, we digitized potential asperity shapes outlined by microseismicity, to then check whether prescribing them in the inversion significantly worsens the data fit. To explore the size of these possible asperities, we considered three possibilities for their geometry towards the trench: 1) minimum sized asperities, with their limits inside of the seismically active area; 2) intermediate-sized asperities, with their limits in the center of the seismicity structures; 3) maximum sized asperities extending all the way up to the trench (see Figure 8a). For our constrained inversions, we then fixed the grid nodes located inside these asperity realizations (Figure 8b) to different coupling values, only inverting for the optimal distribution of interplate coupling on the remainder of grid nodes. This test is mainly designed to check the sensitivity of the inversions to the assumption of differently sized locked patches covering the along-strike extent of the seismicity features we observe. Given the small along-strike gaps between the single asperities and the low spatial resolution of the inversion, our setup can not evaluate whether three discrete patches or a single, elongated one of roughly the same size is present.

In a first run, we fixed the nodes from the different asperity estimates to full coupling. Fixing them excludes these nodes from the optimization process. All other inversion parameters, such as the utilized data or Green's Functions, were the same as for the

323 unconstrained inversion, but since the number of free parameters differed, we determined
 324 new optimal smoothing parameters (β). In order to compare the results of these inver-
 325 sions to the unconstrained inversion, we assessed their statistical significance using the
 326 Bayesian Information Criterion (BIC; Schwarz, 1978). The BIC allows a comparison be-
 327 tween models with different numbers of parameters; the model with a lower BIC should
 328 be preferred. Assuming Gaussian data errors and omitting a constant term, the BIC can
 329 be expressed as

$$BIC = \chi^2 + M \ln(N), \quad (1)$$

330 where N is the number of data points, M the number of parameters and

$$\chi^2 = (\mathbf{d} - \mathbf{G}\hat{\mathbf{m}})^T \mathbf{C}_d^{-1} (\mathbf{d} - \mathbf{G}\hat{\mathbf{m}}) \quad (2)$$

331 is the chi-square misfit. Here, \mathbf{d} and $\hat{\mathbf{m}}$ are the data and optimal parameter vectors, re-
 332 spectively; and \mathbf{G} is the GFs matrix. It is clear from Equation 1 that the BIC will trade-
 333 off model complexity (quantified by M) with misfit (quantified by χ^2). We assumed a
 334 diagonal data covariance matrix \mathbf{C}_d , that is, no correlations are prescribed between data
 335 errors. The elements of \mathbf{C}_d are σ_i^2 , where σ_i is the error for the i -th datum. We assume
 336 that data errors are dominant and assign σ_i to the GPS measurement errors.

337 When assuming full locking, the largest asperity size that extends all the way to
 338 the trench receives a BIC similar to (very slightly lower than) the unconstrained inver-
 339 sion, whereas both other geometries are clearly preferred (i.e. have a lower BIC) com-
 340 pared to the unconstrained inversion (see Figures 8 and 9). We also varied the prescribed
 341 locking degree for the three asperity parameterizations. For each series of inversions with
 342 the same asperity size, the number of parameters is constant, so that variations of the
 343 BIC are purely due to differences in the χ^2 misfit. For all three asperity realizations, a
 344 clear preference of higher locking degrees is visible from the BIC plot. When the same
 345 number of nodes is fixed elsewhere along-strike, the BIC minimum is situated at a sig-
 346 nificantly lower locking percentage (Figure S5) and is less pronounced than the overall
 347 minimum obtained with the original asperity configuration. Moreover, assuming high
 348 locking (>0.8) leads to a BIC larger than for the unconstrained inversion in this setup.
 349 This indicates that the data are sensitive to the along-strike location of highly locked re-
 350 gions, with the location derived from microseismicity being preferred.

351 The minima for the three asperity sizes are situated at locking values of 0.68 (max-
 352 imum asperities), 0.74 (intermediate asperities) and 0.78 (minimum asperities). The global
 353 minimum BIC is reached by the largest asperity realization (i.e. with the largest num-
 354 ber of fixed parameters), which likely implies that the inversion is underdetermined and
 355 a reduction of free parameters is preferred. Comparing data misfits and BIC values, it
 356 appears that a number of scenarios including highly coupled asperities inside the half-
 357 ellipses outlined by the earthquakes can be fit well by the GPS data. Note that RMS
 358 data misfits of the optimum constrained models (Figure 8c) are nearly identical to the
 359 unconstrained inversion (3.73 mm/yr). While the unconstrained model shows a locking
 360 distribution with regions of higher locking that coincides with the region of elevated back-
 361 ground microseismicity at depths of 30-45 km (especially around 32°S), the data can be
 362 fit equally well by models that concentrate coupling further updip, inside the asperity
 363 shapes we introduced. Note that some features of the unconstrained inversion in Fig-
 364 ure 9 also show up in the constrained inversion, for instance the highly locked patch on
 365 the deeper part of the plate interface north of $\sim 30.5^\circ\text{S}$. This likely indicates that such
 366 a feature is required by the GPS data.

367 6 Discussion

368 Our unconstrained GPS inversion for interplate locking has demonstrated that the
 369 GPS data do not require highly coupled regions coincident with the seismicity half-ellipses
 370 (Section 4). However, the prescription of such features yields data fits comparable to the
 371 unconstrained inversion, and our calculated BICs indicate that models with prescribed

372 elevated locking inside the seismicity half-ellipses are preferred. This means that the GPS
373 data clearly do not provide evidence against the existence of such highly locked patches
374 coincident with the aseismic zones within the half-ellipses. Taken together with recently
375 presented evidence from Northern Chile, where a similar microseismicity pattern pre-
376 ceded the 2014 M_w 8.1 Iquique earthquake (Schurr et al., 2020), we think our observa-
377 tions hint at a set of three adjacent highly coupled “asperities” that are present along
378 the Central Chilean margin.

379 Since our conceptual model hinges on the assertion that the vast majority of the
380 seismicity depicted in Figure 3b occurred on the plate interface, we first discuss the in-
381 herent uncertainties and the robustness of our seismicity observations (Section 6.1). Af-
382 ter this, we present a conceptual interpretation of possibly ongoing processes on the Cen-
383 tral Chile megathrust (Section 6.2) and discuss the temporal evolution of their seismic-
384 ity signatures (Section 6.3).

385 6.1 Catalog uncertainties and robustness of seismicity observations

386 We processed raw seismic data from Central Chile and extracted 8750 events at
387 depths shallower than 60 km inside the time interval 04/2014 to 12/2018. Epicenters of
388 these earthquakes form a pattern of three half-ellipse shapes, open towards the trench
389 and oriented with their long axes in trench-parallel direction (Figures S4, 3). Although
390 catalog completeness can be expected to decay offshore, analysis of retrieved magnitudes
391 (Figure S3), especially of events within the “separators” and the outer rise seismicity west
392 of the trench, shows that we should have retrieved any events with $M > 3$ inside the aseis-
393 mic interiors of the half-ellipses.

394 The vast majority of event hypocenters are located within 10 km vertical distance
395 from the plate interface according to slab2 (Hayes et al., 2018, see Figure 2), with the
396 largest event numbers situated 3-5 km below the plate interface (Figure 5). Focal mech-
397 anisms uniformly show low-angle thrusting compatible with displacement along the ~ 20 -
398 25° dipping plate interface. Moreover, most of the seismicity during the Illapel and Val-
399 paraíso earthquake sequences, which were previously interpreted to have largely occurred
400 on the plate interface (e.g. Lange et al., 2016; S. Ruiz et al., 2017), also locates a sim-
401 ilar distance below the slab2 plate interface. This may either indicate that slab2 has an
402 offset of ~ 3 -5 km in this region, or that the utilized velocity model yields locations that
403 are systematically 3-5 km too deep. Also note that estimated relative location uncertainty
404 in the vertical direction, a measure that does not include possible bias due to velocity
405 model misfit, is on the order of 4 km (Figure S1).

406 Based on these considerations, we believe that a vast majority of the events that
407 form the half-ellipses occurred on the plate interface, and that the seismicity presented
408 in Figure 3 largely occurs in response to active processes there. Unlike the study of Schurr
409 et al. (2020) for the Iquique earthquake, we can not clearly show such an ellipse pattern
410 forming directly before a major earthquake. Due to sparse station coverage in the years
411 2014/2015, our catalog does not show much seismicity before the Illapel earthquake and
412 is instead dominated by seismicity in the years 2016-2018 (Figure 4). Thus, the half-ellipse
413 surrounding the slip distribution of the Illapel earthquake in Figure 3 features nearly ex-
414 clusively aftershock seismicity. However, analysis of seismicity from the CSN catalog (Barrientos,
415 2018) in the years before the Illapel earthquake (Figure 10) shows that the along-strike
416 seismicity “separators” that frame the Illapel earthquake to the north and south in our
417 Figure 3 were likely already active before 2015 (the southern one is clearly present, the
418 northern one less clear). This could imply that a late interseismic seismicity pattern akin
419 to the one shown by Schurr et al. (2020) also preceded the Illapel earthquake. While the
420 pre-event seismicity signature of the Iquique and Illapel earthquakes may thus have been
421 similar throughout most of the late interseismic stage, they clearly differ for the last weeks
422 before the events. In the case of the 2014 Iquique earthquake, a two-week foreshock se-
423 quence outlined the updip end of the later main shock rupture, effectively closing the
424 seismicity ellipse (Schurr et al., 2020). Additionally, precursory aseismic slip was reported

425 in the months leading up to the Iquique earthquake (S. Ruiz et al., 2014; Kato et al., 2016;
426 Socquet et al., 2017). No such foreshock sequence or precursory activity was observed
427 for the Illapel earthquake. The reason for this discrepancy may lie in the different up-
428 dip extents of the main shock ruptures. While the Iquique earthquake reached its up-
429 dip termination at ~ 20 km depth (Duputel et al., 2015), there is evidence that the Il-
430 lapel earthquake rupture went significantly further updip and may have extended all the
431 way to the trench (Tilman et al., 2016; Melgar et al., 2016).

432 **6.2 Processes on the Central Chilean plate interface outlined by seis-** 433 **micity**

434 We have retrieved half-ellipse seismicity patterns on the Central Chile megathrust
435 that may outline regions of elevated interplate coupling (“asperities”). Similar predic-
436 tions and observations of a half-ellipse shape of microseismicity around a highly coupled
437 region during the interseismic stage of the seismic cycle have been shown and discussed
438 in Dmowska and Li (1982) and Schurr et al. (2020) for the case of a single asperity. Our
439 present results may be an extension of this case to a setup of three along-strike adjacent
440 asperities. In the interseismic period, microseismicity on the plate interface is mostly driven
441 by creep processes, and hence confined to regions that are not perfectly coupled (i.e. par-
442 tially creeping). Multi-scale heterogeneity on the fault surface means that small patches
443 of stick-slip motion will always be present in predominantly creeping regions, leading to
444 creep-driven microseismicity. Highly coupled regions on the megathrust, in contrast, are
445 largely aseismic in the interseismic period, but produce stress concentrations along their
446 downdip edges (Moreno et al., 2018; Schurr et al., 2020). At some point in the interseis-
447 mic stage of the seismic cycle, stress along the asperity’s downdip edge reaches a crit-
448 ical threshold, whereupon creep processes that cause microseismicity likely set in (see
449 schematic model in Figure S6).

450 While the buildup of shear traction at the downdip end of highly coupled areas on
451 the megathrust provides an explanation for the observed band of microseismicity at depths
452 of 30–45 km, the seismicity “separators” between aseismic regions on the shallow megath-
453 rust (Figure 3b) require a different explanation. Understanding why and where these sep-
454 arators occur is crucial, since they appear to prescribe, or at least image, along-strike
455 segmentation of the Central Chilean plate interface. Along-strike changes in plate inter-
456 face behaviour are thought to be primarily controlled by plate interface roughness, which
457 is often a consequence of the subduction of seafloor relief (Bassett & Watts, 2015; van
458 Rijnsingen et al., 2019). Features like ridges or fracture zones on the downgoing plate may
459 also be more hydrated than ordinary oceanic crust, which can cause elevated pore fluid
460 pressure leading to reduced interplate coupling on the megathrust (Moreno et al., 2014).
461 Clearly identifiable seafloor features, the CFZ and JFR (Figures 1, 3), likely acted as de-
462 limiters of the 2015 Illapel earthquake (Figure 3b; Tilman et al., 2016; Lange et al., 2016;
463 Poli et al., 2017). The microseismicity extending to shallow depths we observe both north
464 and south of the Illapel rupture (Figure 3b,c) could thus be linked to the ongoing sub-
465 duction of these features. The southernmost separator, located at $\sim 33^\circ\text{S}$, is observed where
466 the San Antonio seamount is currently being subducted (J. Ruiz et al., 2018). We note
467 that while the separator just north of 32°S appears to roughly coincide with the north-
468 ern edge of the JFR’s projection, the entire JFR is much wider and extends across most
469 of the central seismicity half-ellipse we observe, a region we associate with high coupling.
470 Since we do not know the properties of the already subducted continuation of the JFR,
471 which is a heterogeneous feature offshore (Figure 1), it is possible that the separator near
472 32°S represents a specific feature (e.g. one or several seamounts) on the already subducted
473 JFR, or that the edge of the ridge is more efficient at lowering interplate coupling than
474 its center.

475 Increased lower plate roughness and/or higher pore fluid pressure on the plate inter-
476 face usually leads to reduced interplate coupling and thus to a larger proportion of
477 aseismic creep (Wang & Bilek, 2014). This fits our observation of more repeating earth-

478 quakes in the separators compared to other regions (Figure 3b,c; also see Poli et al., 2017;
479 S. Ruiz et al., 2017). Events with highly similar waveforms are a consequence of ongoing
480 aseismic creep processes that drive seismic slip on small coupled patches along the
481 heterogeneous plate interface (Nadeau & McEvelly, 1999; Uchida & Bürgmann, 2019).
482 While available maps of interplate coupling (Figure 6, Métois et al., 2012) have insufficient
483 resolution to show reduced coupling along such narrow segments in our study area
484 (Figure 7), the region north of the 2015 Illapel earthquake showcases larger-scale decreased
485 interplate locking accompanied by widespread seismicity (including repeaters) along most
486 of the plate interface (Figure 3b,c). Seismicity along the separators is episodic (Figure
487 3c) and mostly part of major earthquake sequences (Illapel, Valparaíso). However, there
488 is evidence for swarm-like earthquake sequences north and south of the later Illapel rupture
489 in the decades before its rupture (Poli et al., 2017) as well as at $\sim 33^\circ\text{S}$ in the years
490 before the Maule earthquake (Holtkamp & Brudzinski, 2014). Both separators can be
491 recognized in seismicity plots of the CSN earthquake catalog before 2014 (Figure 10).
492 Moreover, some repeating earthquakes are observed from 04/2014 (i.e. before Illapel) in
493 both separators (Figure 3c), and the area of the 2017 Valparaíso earthquake was activated
494 during the Illapel sequence in 2015. The 2017 Valparaíso sequence itself was preceded
495 by transient deformation recognized in GPS data as well as a foreshock sequence
496 (S. Ruiz et al., 2017). North of our study region, the 2020 Atacama seismic sequence,
497 located in a narrow region of low interplate coupling at the southern edge of where the
498 Copiapo Ridge enters the subduction (Klein et al., 2021), may present another more recent
499 example of episodic seismic activity along a possible separator.

500 We thus think that the seismicity separators we observe represent areas of locally
501 decreased interplate coupling and thus increased aseismic creep along the plate interface,
502 often prescribed by features on the incoming oceanic plate. They are intermittently active
503 during the interseismic stage and more strongly active in the postseismic stage of
504 one of the adjacent asperities, when their activity is driven by postseismic slip and possibly
505 stress concentrations at the along-strike terminations of the main shock rupture.
506 Given a long enough observation timespan in the interseismic period, the overall seismicity
507 distribution should resemble the postseismic one (compare the half-ellipse outlined by
508 Illapel aftershocks to the one south of it; Figure S4), which would imply that the localized
509 lows in interseismic coupling that define these separators are stable throughout the seismic
510 cycle and mainly due to structure on the downgoing plate (as also argued in Agurto-Detzel et al.,
511 2019). It is important to better characterize such regions, for instance through the deployment
512 of dense GPS networks (ideally on- and offshore), since their widths relative to the adjacent
513 highly coupled areas and their coupling properties determine their efficiency as barriers to large
514 earthquakes (e.g. Corbi et al., 2017).

515 **6.3 Mogi Doughnuts and the temporal evolution of seismicity patterns**

516 Pre-seismic quiescence in an earthquake's rupture area, accompanied by increased
517 seismicity levels in a ring or half-ring shape around it, has been first observed more than
518 five decades ago (Mogi, 1969, 1979; Kanamori, 1981). Although such "Mogi doughnuts"
519 have later also been predicted with mechanical models (Dmowska & Li, 1982) and observed
520 in rock mechanics experiments (Goebel et al., 2012), only very few clear observations
521 of Mogi doughnuts have been made to date (e.g. Schurr et al., 2020). In contrast,
522 observations of aftershock seismicity surrounding the main shock slip areas are well established
523 (Das & Henry, 2003) and often ascribed to stress concentrations at the rupture
524 limits.

525 We think that one reason for the scarce observations of Mogi Doughnuts may lie
526 in the temporal evolution of seismicity, which appears to be markedly different between
527 the downdip edges of highly coupled regions and the along-strike separators. Interseismic
528 loading of asperities naturally results in concentrations of shear traction at their downdip
529 edges (e.g. Moreno et al., 2018). Microseismicity at these stress concentrations likely only
530 commences once a stress threshold level has been reached. From that time onwards, seis-

531 micity in these regions will appear to be continuous (Figure 3c). Observations of such
532 bands of seismicity located around the downdip termination of interseismic locking are
533 not uncommon (e.g. Feng et al., 2012; Ader et al., 2012; Yarcé et al., 2019). The along-
534 strike separators that subdivide the shallower megathrust into single asperities, in con-
535 trast, are only active in episodically occurring bursts (Figure 3c), most prominently when
536 activated by nearby events (similar to observations of Schurr et al., 2020). This means
537 that for relatively short-term seismicity studies like ours, such separators can easily be
538 missed. Unlike the band of deeper interface seismicity, they feature large amounts of re-
539 peating earthquakes that are proxies for ongoing aseismic creep. Long-term studies of
540 repeating earthquakes have shown clusters of such events downdip and at the along-strike
541 terminations of later megathrust earthquakes (e.g. Uchida & Matsuzawa, 2013). These
542 observations may be due to the erosion of coupled asperities by creep processes that have
543 been shown in rate-and-state simulations (Mavrommatis et al., 2017; Jiang & Lapusta,
544 2017).

545 Immediately after a main shock rupture on an adjacent segment occurs, its along-
546 strike separators will show high rates of seismicity (see Figure 3c) due to induced stress
547 concentrations at the rupture edges as well as high-rate aseismic processes in the post-
548 seismic stage (Perfettini et al., 2010). Thus, a clearer and easier identification of such
549 separators during aftershock series is possible due to higher seismicity rates. We think
550 that the general pattern of microseismicity is, however, similar for the postseismic and
551 the interseismic stage of the seismic cycle, because the features that prescribe the inter-
552 seismic seismicity pattern (regions of only partial coupling acting as along-strike sepa-
553 rators and the downdip edges of asperities that concentrate stresses) also prescribe the
554 edges of the main shock rupture. As both aftershock series and postseismic afterslip to
555 first order occur in the region surrounding main shock slip (e.g. Das & Henry, 2003; Per-
556 fettini et al., 2010), both creep-driven or stress-driven aftershock seismicity should out-
557 line patterns that are to first order similar to what emerges when a sufficiently large pro-
558 portion of the interseismic stage is observed. A recent example for the postseismic ac-
559 tivation of along-strike separators is the 2016 M_w 7.8 Pedernales earthquake in Ecuador,
560 where the main shock was located on the deeper part of the megathrust, but activated
561 three narrow seismicity separators outlining largely aseismic regions on the presumably
562 unruptured shallow part of the megathrust (Agurto-Detzel et al., 2019; Soto-Cordero et
563 al., 2020). As in Central Chile, these features can be correlated with incoming seafloor
564 relief.

565 For Central Chile, our results imply that two adjacent asperities are possibly present
566 between the rupture areas of the 2015 Illapel and the 2010 Maule earthquake (see Fig-
567 ure 3b), and may have accumulated stress for nearly 300 years. Given that the 2014 Iquique
568 earthquake was preceded by a similar pattern (Schurr et al., 2020), we believe that our
569 observations could help to constrain the seismic potential of the region. The imaged bar-
570 rier between the two potential asperities, highlighted by the 2017 Valparaíso earthquake
571 sequence (Figure 3b,c), likely mechanically controls whether they will rupture jointly or
572 individually.

573 7 Conclusions

574 We observe three trenchward open seismicity half-ellipses on the Central Chile megath-
575 rust when analyzing the time period 2014-2018. They consist of a trench-parallel, along-
576 strike continuous band of plate interface microseismicity at depths of 30-45 km, as well
577 as two along-strike separators where seismicity extends significantly further towards the
578 trench. The resolution of available GPS data does not allow us to independently verify
579 whether these half-ellipses correspond to strongly coupled patches on the megathrust.
580 However, by prescribing such highly locked “asperities” in constrained inversions of GPS
581 data, we show that their existence is one possible way to explain the observed upper plate
582 deformation in Central Chile.

583 According to our interpretation, continued interseismic loading of strongly coupled
 584 asperities leads to gradual buildup of stress concentrations along their down-dip edges.
 585 These stress concentrations eventually cause aseismic creep driving continuous micro-
 586 seismicity from some time in the interseismic stage onwards. The narrow along-strike
 587 separators between asperities appear to correspond to regions of increased roughness and/or
 588 hydration on the incoming Nazca Plate, likely effecting elevated creep that occurs in tran-
 589 sient bursts and drives swarm-like earthquake sequences. This implies that valuable in-
 590 formation about the segmentation of megathrust faults can be obtained from the anal-
 591 ysis of seismicity distributions, provided that the analyzed region has already overcome
 592 the stress threshold after which the microseismicity in the down-dip band develops, and
 593 that the observational timespan is long enough to capture the episodic activity of along-
 594 strike separators. We further speculate that incorporating seismicity information into
 595 future locking inversion approaches may be a way to improve spatial resolution of GPS-
 596 based locking maps, especially in the badly resolved offshore regions.

597 Acknowledgments

598 We thank the editor Michael Bostock, Anne Tréhu and one anonymous reviewer for com-
 599 ments and suggestions that helped to improve the manuscript. We also thank review-
 600 ers of a previous version of the article for their comments, and Bernd Schurr for valu-
 601 able discussions. The seismic waveform data that was used to compile the earthquake
 602 catalog was retrieved from the IRIS webpage (<http://www.ds.iris.edu/ds/nodes/dmc/>),
 603 and came from the networks C1 (Universidad de Chile, 2013), C (no DOI available), II
 604 (Scripps Institution Of Oceanography, 1986), G (Institut de Physique du Globe de Paris
 605 & Ecole et Observatoire des Sciences de la Terre de Strasbourg (EOST), n.d.) and WA
 606 (Universidad Nacional de San Juan Argentina, 1958). Moment tensors shown in Figure
 607 3 were retrieved from the globalCMT (<https://www.globalcmt.org/>) and GEOFON ([https://geofon.gfz-
 608 potsdam.de/eqinfo/](https://geofon.gfz-potsdam.de/eqinfo/)) databases. Seismic data processing was done with ObsPy (Beyreuther
 609 et al., 2010), figures were plotted with the Matplotlib (Hunter, 2007) and Basemap (<https://matplotlib.org/basemap>)
 610 libraries.

The seismicity catalog presented in this article is available on Zenodo.org (<https://dx.doi.org/10.5281/zenodo>)

611 C.S. has received funding from the European Research Council (ERC) under the
 612 European Unions Horizon 2020 research and innovation programme (ERC Starting grant
 613 MILESTONE, StG2020-947856). M.M. acknowledges support from the Millennium Nu-
 614 cleus CYCLO (The Seismic Cycle Along Subduction Zones) funded by the Millennium
 615 Scientific Initiative (ICM) of the Chilean Government Grant NC160025, Chilean National
 616 Fund for Development of Science and Technology (FONDECYT) grant 1181479, the ANID
 617 PIA Anillo ACT192169, and CONICYT/FONDAP 15110017. R.B. acknowledges fund-
 618 ing from ANID, Chile through grant ANID/FONDECYT/3190322.
 619

620 References

- 621 Aagaard, B. T., Knepley, M. G., & Williams, C. A. (2013). A domain decomposition
 622 approach to implementing fault slip in finite-element models of quasi-static and
 623 dynamic crustal deformation. *Journal of Geophysical Research: Solid Earth*,
 624 *118*(6), 3059–3079. doi: 10.1002/jgrb.50217
- 625 Ader, T., Avouac, J.-P., Liu-Zeng, J., Lyon-Caen, H., Bollinger, L., Galetzka, J.,
 626 ... Flouzat, M. (2012). Convergence rate across the Nepal Himalaya and
 627 interseismic coupling on the Main Himalayan Thrust: Implications for seismic
 628 hazard. *Journal of Geophysical Research: Solid Earth*, *117*(4), 1–16. doi:
 629 10.1029/2011JB009071
- 630 Agurto-Detzel, H., Font, Y., Charvis, P., Régnier, M., Rietbrock, A., Ambrois, D.,
 631 ... Soto-Cordero, L. (2019). Ridge subduction and afterslip control aftershock
 632 distribution of the 2016 Mw 7.8 Ecuador earthquake. *Earth and Planetary
 633 Science Letters*, *520*, 63–76. Retrieved from <https://doi.org/10.1016/>

- 634 j.epsl.2019.05.029 doi: 10.1016/j.epsl.2019.05.029
- 635 Anderson, M., Alvarado, P., Zandt, G., & Beck, S. L. (2007). Geometry and
636 brittle deformation of the subducting Nazca Plate, Central Chile and
637 Argentina. *Geophysical Journal International*, 171(1), 419–434. doi:
638 10.1111/j.1365-246X.2007.03483.x
- 639 Angermann, D., Klotz, J., & Reigber, C. (1999). Space-geodetic estimation of the
640 Nazca-South America Euler vector. *Earth and Planetary Science Letters*,
641 171(3), 329–334. doi: 10.1016/S0012-821X(99)00173-9
- 642 Barrientos, S. (2018). The Seismic Network of Chile. *Seismological Research Let-*
643 *ters*, 89(2A), 467–474. Retrieved from [https://pubs.geoscienceworld.org/](https://pubs.geoscienceworld.org/ssa/srl/article/89/2A/467/528198/The-Seismic-Network-of-Chile)
644 [ssa/srl/article/89/2A/467/528198/The-Seismic-Network-of-Chile](https://pubs.geoscienceworld.org/ssa/srl/article/89/2A/467/528198/The-Seismic-Network-of-Chile) doi:
645 10.1785/0220160195
- 646 Barrientos, S., Vera, E., Alvarado, P., & Monfret, T. (2004). Crustal seismicity in
647 central Chile. *Journal of South American Earth Sciences*, 16(8), 759–768. doi:
648 10.1016/j.jsames.2003.12.001
- 649 Bassett, D., & Watts, A. B. (2015). Gravity anomalies, crustal structure, and
650 seismicity at subduction zones: 1. Seafloor roughness and subducting relief.
651 *Geochemistry, Geophysics, Geosystems*, 16, 1508–1540. Retrieved from
652 <http://www.tandfonline.com/doi/full/10.2753/RP01061-0405330447>
653 doi: 10.1002/2014GC005685.Key
- 654 Béjar-Pizarro, M., Socquet, A., Armijo, R., Carrizo, D., Genrich, J., & Simons,
655 M. (2013). Andean structural control on interseismic coupling in the North
656 Chile subduction zone. *Nature Geoscience*, 6(6), 462–467. Retrieved from
657 <http://dx.doi.org/10.1038/ngeo1802> doi: 10.1038/ngeo1802
- 658 Benavente, R., Cummins, P. R., & Dettmer, J. (2016). Rapid automated W-phase
659 slip inversion for the Illapel great earthquake (2015, Mw = 8.3). *Geophysical*
660 *Research Letters*, 43(5), 1910–1917. doi: 10.1002/2015GL067418
- 661 Beyreuther, M., Barsch, R., Krischer, L., Megies, T., Behr, Y., & Wassermann, J.
662 (2010). ObsPy: A Python Toolbox for Seismology. *Seismological Research Let-*
663 *ters*, 81(3), 530–533. Retrieved from [https://pubs.geoscienceworld.org/](https://pubs.geoscienceworld.org/srl/article/81/3/530-533/143693)
664 [srl/article/81/3/530-533/143693](https://pubs.geoscienceworld.org/srl/article/81/3/530-533/143693) doi: 10.1785/gssrl.81.3.530
- 665 Bletery, Q., Thomas, A. M., Rempel, A. W., Karlstrom, L., Sladen, A., & De
666 Barros, L. (2016). Mega-earthquakes rupture flat megathrusts. *Science*,
667 354(6315), 1027–1031. doi: 10.1126/science.aag0482
- 668 Bravo, F., Koch, P., Riquelme, S., Fuentes Serrano, M., & Campos, J. (2019).
669 Slip Distribution of the 1985 Valparaíso Earthquake Constrained with Seis-
670 mic and Deformation Data. *Seismological Research Letters*, 9, 1–9. doi:
671 10.1785/0220180396
- 672 Brooks, B., Bevis, M., Smalley, R., Kendrick, E., Manceda, R., Lauría, E., ...
673 Araujo, M. (2003). Crustal motion in the Southern Andes (26-36S): Do
674 the Andes behave like a microplate? *Geochemistry, Geophysics, Geosystems*,
675 4(10), 1–14. doi: 10.1029/2003GC000505
- 676 Bürgmann, R., Kogan, M. G., Steblov, G. M., Hilley, G., Levin, V., & Apel, E.
677 (2005). Interseismic coupling and asperity distribution along the Kamchatka
678 subduction zone. *Journal of Geophysical Research*, 110(7), B07405. doi:
679 10.1029/2005JB003648
- 680 Carvajal, M., Cisternas, M., & Catalán, P. A. (2017). Source of the 1730 Chilean
681 earthquake from historical records: Implications for the future tsunami hazard
682 on the coast of Metropolitan Chile. *Journal of Geophysical Research*, 122(5),
683 3648–3660. doi: 10.1002/2017JB014063
- 684 Chlieh, M., Avouac, J.-P., Sieh, K., Natawidjaja, D. H., & Galetzka, J. (2008).
685 Heterogeneous coupling of the Sumatran megathrust constrained by geodetic
686 and paleogeodetic measurements. *Journal of Geophysical Research*, 113(5),
687 B05305. doi: 10.1029/2007JB004981
- 688 Chlieh, M., De Chabalier, J. B., Ruegg, J. C., Armijo, R., Dmowska, R., Cam-

- 689 pos, J., & Feigl, K. L. (2004). Crustal deformation and fault slip during
 690 the seismic cycle in the North Chile subduction zone, from GPS and InSAR
 691 observations. *Geophysical Journal International*, *158*(2), 695–711. doi:
 692 10.1111/j.1365-246X.2004.02326.x
- 693 Chlieh, M., Perfettini, H., Tavera, H., Avouac, J.-P., Remy, D., Nocquet, J. M., ...
 694 Bonvalot, S. (2011). Interseismic coupling and seismic potential along the
 695 Central Andes subduction zone. *Journal of Geophysical Research: Solid Earth*,
 696 *116*(12), B12405. doi: 10.1029/2010JB008166
- 697 Cloos, M. (1992). Thrust-type subduction-zone earthquakes and seamount asperities:
 698 a physical model for seismic rupture. *Geology*, *20*, 601–604.
- 699 Comte, D., & Pardo, M. (1991). Reappraisal of great historical earthquakes in the
 700 northern Chile and southern Peru seismic gaps. *Natural Hazards*, *4*(1), 23–44.
 701 doi: 10.1007/BF00126557
- 702 Contreras-Reyes, E., & Carrizo, D. (2011). Control of high oceanic features and
 703 subduction channel on earthquake ruptures along the Chile-Peru subduc-
 704 tion zone. *Physics of the Earth and Planetary Interiors*, *186*(1-2), 49–58.
 705 Retrieved from <http://dx.doi.org/10.1016/j.pepi.2011.03.002> doi:
 706 10.1016/j.pepi.2011.03.002
- 707 Corbi, F., Funicello, F., Brizzi, S., Lallemand, S., & Rosenau, M. (2017).
 708 Control of asperities size and spacing on seismic behavior of subduction
 709 megathrusts. *Geophysical Research Letters*, *44*(16), 8227–8235. doi:
 710 10.1002/2017GL074182
- 711 Das, S., & Henry, C. (2003). Spatial relation between main earthquake slip and its
 712 aftershock distribution. *Reviews of Geophysics*, *41*(3), 1013. doi: 10.1029/
 713 2002RG000119
- 714 Di Stefano, R., Aldersons, F., Kissling, E., Baccheschi, P., Chiarabba, C., & Giar-
 715 dini, D. (2006). Automatic seismic phase picking and consistent observation
 716 error assessment: Application to the Italian seismicity. *Geophysical Journal*
 717 *International*, *165*(1), 121–134. doi: 10.1111/j.1365-246X.2005.02799.x
- 718 Diehl, T., Deichmann, N., Kissling, E., & Husen, S. (2009). Automatic S-wave
 719 picker for local earthquake tomography. *Bulletin of the Seismological Society of*
 720 *America*, *99*(3), 1906–1920. doi: 10.1785/0120080019
- 721 Dmowska, R., & Li, V. C. (1982). A mechanical model of precursory source pro-
 722 cesses for some large earthquakes. *Geophysical Research Letters*, *9*(4), 393–396.
 723 doi: 10.1029/GL009i004p00393
- 724 Duputel, Z., Jiang, J., Jolivet, R., Simons, M., Rivera, L., Ampuero, J. P., ... Min-
 725 son, S. E. (2015). The Iquique earthquake sequence of April 2014: Bayesian
 726 modeling accounting for prediction uncertainty. *Geophysical Research Letters*,
 727 *42*(19), 7949–7957. doi: 10.1002/2015GL065402
- 728 Feng, L., Newman, A. V., Protti, M., Gonzalez, V., Jiang, Y., & Dixon, T. (2012).
 729 Active deformation near the Nicoya Peninsula, northwestern Costa Rica,
 730 between 1996 and 2010: Interseismic megathrust coupling. *Journal of Geophys-
 731 ical Research: Solid Earth*, *117*(6), 1–23. doi: 10.1029/2012JB009230
- 732 Fujiwara, T., Kodaira, S., No, T., Kaiho, Y., Takahashi, N., & Kaneda, Y. (2011).
 733 The 2011 Tohoku-oki Earthquake : Displacement reaching the trench axis. *Sci-
 734 ence*, *334*, 1240.
- 735 GEBCO_Compilation_Group. (2020). *GEBCO 2020 Grid*. doi: 10.5285/a29c5465
 736 -b138-234d-e053-6c86abc040b9
- 737 Goebel, T. H., Becker, T. W., Schorlemmer, D., Stanchits, S., Sammis, C. G., Ry-
 738 backi, E., & Dresen, G. (2012). Identifying fault heterogeneity through map-
 739 ping spatial anomalies in acoustic emission statistics. *Journal of Geophysical*
 740 *Research*, *117*(3), 1–18. doi: 10.1029/2011JB008763
- 741 Hayes, G. P., Moore, G., Portner, D. E., Hearne, M., Flamme, H., Furtney, M., &
 742 Smoczyk, G. M. (2018). Slab2, a comprehensive subduction zone geometry
 743 model. *Science*, *362*(6410), 58–61. doi: 10.1126/science.aat4723

- 744 Hayes, G. P., Wald, D. J., & Johnson, R. L. (2012). Slab1.0: A three-dimensional
745 model of global subduction zone geometries. *Journal of Geophysical Research*,
746 *117*(1), 1–15. doi: 10.1029/2011JB008524
- 747 Holtkamp, S., & Brudzinski, M. R. (2014). Megathrust earthquake swarms indicate
748 frictional changes which delimit large earthquake ruptures. *Earth and Plan-*
749 *etary Science Letters*, *390*, 234–243. Retrieved from [http://dx.doi.org/](http://dx.doi.org/10.1016/j.epsl.2013.10.033)
750 [10.1016/j.epsl.2013.10.033](http://dx.doi.org/10.1016/j.epsl.2013.10.033) doi: 10.1016/j.epsl.2013.10.033
- 751 Hunter, J. D. (2007). Matplotlib: A 2D graphics environment. *Computing in Science*
752 *and Engineering*, *9*(3), 90–95. doi: 10.1109/MCSE.2007.55
- 753 Ide, S., Baltay, A., & Beroza, G. C. (2011). Shallow dynamic overshoot and en-
754 ergetic deep rupture in the 2011 M_w 9.0 Tohoku-Oki earthquake. *Science*,
755 *332*(6036), 1426–1429. doi: 10.1126/science.1207020
- 756 Institut de Physique du Globe de Paris & Ecole et Observatoire des Sciences de la
757 Terre de Strasbourg (EOST). (n.d.). *GEOSCOPE - French Global Network of*
758 *broadband seismic stations*. doi: 10.18715/GEOSCOPE.G
- 759 Jiang, J., & Lapusta, N. (2017). Connecting depth limits of interseismic lock-
760 ing, microseismicity, and large earthquakes in models of long-term fault
761 slip. *Journal of Geophysical Research: Solid Earth*, *122*(8), 6491–6523. doi:
762 [10.1002/2017JB014030](http://dx.doi.org/10.1002/2017JB014030)
- 763 Kanamori, H. (1981). The Nature of Seismicity Patterns Before Large Earthquakes.
764 In *Earthquake prediction* (pp. 1–19). doi: 10.1029/me004p0001
- 765 Kato, A., Fukuda, J., Kumazawa, T., & Nakagawa, S. (2016). Accelerated nucleation
766 of the 2014 Iquique, Chile Mw 8.2 Earthquake. *Scientific Reports*, *6*(December
767 2015), 1–9. Retrieved from <http://dx.doi.org/10.1038/srep24792> doi: 10
768 [.1038/srep24792](http://dx.doi.org/10.1038/srep24792)
- 769 Kendrick, E., Bevis, M., Smalley, R., Brooks, B., Vargas, R. B., Lauría, E., & Fortes,
770 L. P. S. (2003). The Nazca-South America Euler vector and its rate of
771 change. *Journal of South American Earth Sciences*, *16*(2), 125–131. doi:
772 [10.1016/S0895-9811\(03\)00028-2](http://dx.doi.org/10.1016/S0895-9811(03)00028-2)
- 773 Kissling, E., Ellsworth, W. L., Eberhart-Phillips, D., & Kradolfer, U. (1994). Initial
774 reference models in local earthquake tomography. *Journal of Geophysical Re-*
775 *search*, *99*(B10), 19,635–19,646.
- 776 Klein, E., Potin, B., Pasten-Araya, F., Tissandier, R., Azua, K., Duputel, Z., ...
777 Vigny, C. (2021). Interplay of seismic and a-seismic deformation during the
778 2020 sequence of Atacama, Chile. *Earth and Planetary Science Letters*, *570*,
779 117081. Retrieved from <https://doi.org/10.1016/j.epsl.2021.117081>
780 doi: 10.1016/j.epsl.2021.117081
- 781 Klotz, J., Khazaradze, G., Angermann, D., Reigber, C., Perdomo, R., & Cifuentes,
782 O. (2001). Earthquake cycle dominates contemporary crustal deformation in
783 Central and Southern Andes. *Earth and Planetary Science Letters*, *193*(3-4),
784 437–446. doi: 10.1016/S0012-821X(01)00532-5
- 785 Lange, D., Geersen, J., Barrientos, S., Moreno, M., Grevemeyer, I., Contreras-Reyes,
786 E., & Kopp, H. (2016). Aftershock seismicity and tectonic setting of the 2015
787 September 16 Mw 8.3 Illapel earthquake, Central Chile. *Geophysical Journal*
788 *International*, *206*(2), 1424–1430. doi: 10.1093/gji/ggw218
- 789 Lange, D., Tilmann, F., Barrientos, S., Contreras-Reyes, E., Methe, P., Moreno, M.,
790 ... Beck, S. L. (2012). Aftershock seismicity of the 27 February 2010 Mw 8.8
791 Maule earthquake rupture zone. *Earth and Planetary Science Letters*, *317-*
792 *318*(February 2010), 413–425. Retrieved from [http://dx.doi.org/10.1016/](http://dx.doi.org/10.1016/j.epsl.2011.11.034)
793 [j.epsl.2011.11.034](http://dx.doi.org/10.1016/j.epsl.2011.11.034) doi: 10.1016/j.epsl.2011.11.034
- 794 Lay, T., & Kanamori, H. (1981). An asperity model for large earthquake sequences.
795 *Earthquake Prediction*, 579–592.
- 796 Lay, T., Kanamori, H., Ammon, C. J., Koper, K. D., Hutko, A. R., Ye, L., ... Rush-
797 ing, T. M. (2012). Depth-varying rupture properties of subduction zone
798 megathrust faults. *Journal of Geophysical Research*, *117*(4), B04311. doi:

799
800
801
802
803
804
805
806
807
808
809
810
811
812
813
814
815
816
817
818
819
820
821
822
823
824
825
826
827
828
829
830
831
832
833
834
835
836
837
838
839
840
841
842
843
844
845
846
847
848
849
850
851
852
853

- 10.1029/2011JB009133
- Li, S., Moreno, M., Bedford, J., Rosenau, M., & Oncken, O. (2015). Revisiting viscoelastic effects on interseismic deformation and locking degree: A case study of the Peru-North Chile subduction zone. *Journal of Geophysical Research*, *120*(6), 4522–4538. doi: 10.1002/2015JB011903
- Lomnitz, C. (2004). Major Earthquakes of Chile: A Historical Survey, 1535–1960. *Seismological Research Letters*, *75*(3), 368–378. doi: 10.1785/gssrl.75.3.368
- Loveless, J. P., & Meade, B. J. (2011). Spatial correlation of interseismic coupling and coseismic rupture extent of the 2011 $M_w = 9.0$ Tohoku-oki earthquake. *Geophysical Research Letters*, *38*(17), 2–6. doi: 10.1029/2011GL048561
- Loveless, J. P., & Meade, B. J. (2016). Two decades of spatiotemporal variations in subduction zone coupling offshore Japan. *Earth and Planetary Science Letters*, *436*, 19–30. Retrieved from <http://dx.doi.org/10.1016/j.epsl.2015.12.033> doi: 10.1016/j.epsl.2015.12.033
- Marot, M., Monfret, T., Pardo, M., Ranalli, G., & Nolet, G. (2013). A double seismic zone in the subducting Juan Fernandez Ridge of the Nazca Plate (32S), central Chile. *Journal of Geophysical Research*, *118*(7), 3462–3475. doi: 10.1002/jgrb.50240
- Mavrommatis, A. P., Segall, P., & Johnson, K. M. (2017). A Physical Model for Interseismic Erosion of Locked Fault Asperities. *Journal of Geophysical Research: Solid Earth*, *122*(10), 8326–8346. doi: 10.1002/2017JB014533
- Melgar, D., Fan, W., Riquelme, S., Geng, J., Liang, C., Fuentes Serrano, M., ... Fielding, E. J. (2016). Slip segmentation and slow rupture to the trench during the 2015, $M_w 8.3$ Illapel, Chile earthquake. *Geophysical Research Letters*, *43*(3), 961–966. doi: 10.1002/2015GL067369
- Métois, M., Socquet, A., & Vigny, C. (2012). Interseismic coupling, segmentation and mechanical behavior of the central Chile subduction zone. *Journal of Geophysical Research: Solid Earth*, *117*(3), B03406. doi: 10.1029/2011JB008736
- Métois, M., Vigny, C., & Socquet, A. (2016). Interseismic Coupling, Megathrust Earthquakes and Seismic Swarms Along the Chilean Subduction Zone (3818S). *Pure and Applied Geophysics*, *173*(5), 1431–1449. doi: 10.1007/s00024-016-1280-5
- Mogi, K. (1969). Some features of recent seismic activity in and near Japan(2): Activity before and after great earthquakes. *Bull. Earthquake Res. Inst. Univ. Tokyo*, *47*, 395–417.
- Mogi, K. (1979). Two kinds of seismic gaps. *Pure and Applied Geophysics*, *117*(6), 1172–1186. doi: 10.1007/BF00876213
- Moreno, M., Haberland, C., Oncken, O., Rietbrock, A., Angiboust, S., & Heidbach, O. (2014). Locking of the Chile subduction zone controlled by fluid pressure before the 2010 earthquake. *Nature Geoscience*, *7*(4), 292–296. doi: 10.1038/ngeo2102
- Moreno, M., Li, S., Melnick, D., Bedford, J., Baez, J. C., Motagh, M., ... Oncken, O. (2018). Chilean megathrust earthquake recurrence linked to frictional contrast at depth. *Nature Geoscience*, *11*(4), 285–290. doi: 10.1038/s41561-018-0089-5
- Moreno, M., Melnick, D., Rosenau, M., Baez, J. C., Klotz, J., Oncken, O., ... Hase, H. (2012). Toward understanding tectonic control on the $M_w 8.8$ 2010 Maule Chile earthquake. *Earth and Planetary Science Letters*, *321–322*, 152–165. Retrieved from <http://dx.doi.org/10.1016/j.epsl.2012.01.006> doi: 10.1016/j.epsl.2012.01.006
- Moreno, M., Melnick, D., Rosenau, M., Bolte, J., Klotz, J., Echtler, H., ... Oncken, O. (2011). Heterogeneous plate locking in the South-Central Chile subduction zone: Building up the next great earthquake. *Earth and Planetary Science Letters*, *305*(3–4), 413–424. Retrieved from <http://dx.doi.org/10.1016/>

- 854 j.epsl.2011.03.025 doi: 10.1016/j.epsl.2011.03.025
- 855 Moreno, M., Rosenau, M., & Oncken, O. (2010). 2010 Maule earthquake slip corre-
856 lates with pre-seismic locking of Andean subduction zone. *Nature*, *467*(7312),
857 198–202. Retrieved from <http://dx.doi.org/10.1038/nature09349> doi: 10
858 .1038/nature09349
- 859 Müller, R. D., Sdrolias, M., Gaina, C., & Roest, W. R. (2008). Age, spreading
860 rates, and spreading asymmetry of the world's ocean crust. *Geochemistry,*
861 *Geophysics, Geosystems*, *9*(4), Q04006. doi: 10.1029/2007GC001743
- 862 Nadeau, R. M., & McEvilly, T. V. (1999). Fault slip rates at depth from recurrence
863 intervals of repeating microearthquakes. *Science*, *285*(5428), 718–721. doi: 10
864 .1126/science.285.5428.718
- 865 Nealy, J. L., Herman, M. W., Moore, G., Hayes, G. P., Benz, H., Bergman, E., &
866 Barrientos, S. (2017). 2017 Valparaíso earthquake sequence and the megath-
867 rust patchwork of central Chile. *Geophysical Research Letters*, *44*(17), 8865–
868 8872. doi: 10.1002/2017GL074767
- 869 Oleskevich, D. A., Hyndman, R. D., & Wang, K. (1999). The updip and downdip
870 limits to great subduction earthquakes: Thermal and structural models of Cas-
871 cadia, south Alaska, SW Japan, and Chile. *Journal of Geophysical Research*,
872 *104*(B7), 14965–14991. doi: 10.1029/1999jb900060
- 873 Pacheco, F., Sykes, L. R., & Scholz, C. H. (1993). Nature of seismic coupling along
874 simple plate boundaries of the subduction type. *Journal of Geophysical Re-*
875 *search*, *98*(B8), 14,133–14,159.
- 876 Perfettini, H., Avouac, J.-P., Tavera, H., Kositsky, A., Nocquet, J. M., Bondoux, F.,
877 ... Soler, P. (2010). Seismic and aseismic slip on the Central Peru megathrust.
878 *Nature*, *465*(7294), 78–81. Retrieved from [http://dx.doi.org/10.1038/](http://dx.doi.org/10.1038/nature09062)
879 [nature09062](http://dx.doi.org/10.1038/nature09062) doi: 10.1038/nature09062
- 880 Poli, P., Jeria, A. M., & Ruiz, S. (2017). The Mw 8.3 Illapel earthquake (Chile):
881 Preseismic and postseismic activity associated with hydrated slab structures.
882 *Geology*, *45*(3), 247–250. doi: 10.1130/G38522.1
- 883 Ramos, V. A., Cristallini, E. O., & Pérez, D. J. (2002). The Pampean flat-slab of
884 the Central Andes. *Journal of South American Earth Sciences*, *15*(1), 59–78.
885 doi: 10.1016/S0895-9811(02)00006-8
- 886 Ramos, V. A., & Folguera, A. (2009). Andean flat-slab subduction through time.
887 *Geological Society, London, Special Publications*, *327*(1), 31–54. doi: 10.1144/
888 sp327.3
- 889 Ruiz, J., Contreras-Reyes, E., Ortega Culaciati, F., & Manríquez, P. (2018). Rup-
890 ture process of the April 24, 2017, Mw 6.9 Valparaíso earthquake from the
891 joint inversion of teleseismic body waves and near-field data. *Physics of the*
892 *Earth and Planetary Interiors*, *279*, 1–14. Retrieved from [https://doi.org/](https://doi.org/10.1016/j.pepi.2018.03.007)
893 [10.1016/j.pepi.2018.03.007](https://doi.org/10.1016/j.pepi.2018.03.007) doi: 10.1016/j.pepi.2018.03.007
- 894 Ruiz, S., Aden-Antoniow, F., Baez, J. C., Otarola, C., Potin, B., del Campo, F., ...
895 Bernard, P. (2017). Nucleation Phase and Dynamic Inversion of the Mw 6.9
896 Valparaíso 2017 Earthquake in Central Chile. *Geophysical Research Letters*,
897 *44*(20), 10,290–10,297. doi: 10.1002/2017GL075675
- 898 Ruiz, S., & Madariaga, R. (2018). Historical and recent large megathrust earth-
899 quakes in Chile. *Tectonophysics*, *733*, 37–56. doi: 10.1016/j.tecto.2018.01.015
- 900 Ruiz, S., Metois, M., Fuenzalida, A., Ruiz, J., Leyton, F., Grandin, R., ... Campos,
901 J. (2014). Intense foreshocks and a slow slip event preceded the 2014 Iquique
902 Mw 8.1 earthquake. *Science*, *345*, 1165–1170.
- 903 Savage, J. C. (1983). A dislocation model of strain accumulation and release at a
904 subduction zone. *Journal of Geophysical Research*, *88*(B6), 4984–4996. doi: 10
905 .1029/JB088iB06p04984
- 906 Schurr, B., Asch, G., Hainzl, S., Bedford, J., Hoechner, A., Palo, M., ... Vilotte,
907 J. P. (2014). Gradual unlocking of plate boundary controlled initia-
908 tion of the 2014 Iquique earthquake. *Nature*, *512*(7514), 299–302. doi:

- 10.1038/nature13681
- 909 Schurr, B., Moreno, M., Tréhu, A. M., Bedford, J., Kummerow, J., Li, S., & Oncken,
910 O. (2020). Forming a Mogi Doughnut in the Years Prior to and Immediately
911 Before the 2014 M8.1 Iquique, Northern Chile, Earthquake. *Geophysical
912 Research Letters*, *47*(16). doi: 10.1029/2020GL088351
- 913 Schwarz, G. (1978). Estimating the dimension of a model. *The Annals of Statistics*,
914 *6*(2), 461–464. doi: 10.1214/aos/1176348654
- 915 Scripps Institution Of Oceanography. (1986). *IRIS/IDA Seismic Network. Inter-
916 national Federation of Digital Seismograph Networks*. doi: [https://doi.org/10.
917 .7914/SN/II](https://doi.org/10.7914/SN/II)
- 918 Sippl, C., Schurr, B., Yuan, X., Mechie, J., Schneider, F. M., Gadoev, M., ... Rad-
919 jabov, N. (2013). Geometry of the Pamir-Hindu Kush intermediate-depth
920 earthquake zone from local seismic data. *Journal of Geophysical Research*,
921 *118*(4), 1438–1457. doi: 10.1002/jgrb.50128
- 922 Socquet, A., Valdes, J. P., Jara, J., Cotton, F., Walpersdorf, A., Cotte, N., ... Nor-
923 abuena, E. (2017). An 8month slow slip event triggers progressive nucleation
924 of the 2014 Chile megathrust. *Geophysical Research Letters*, *44*(9), 4046–4053.
925 doi: 10.1002/2017GL073023
- 926 Soto-Cordero, L., Meltzer, A., Bergman, E., Hoskins, M., Stachnik, J. C., Agurto-
927 Detzel, H., ... Ruiz, M. (2020). Structural Control on Megathrust Rupture
928 and Slip Behavior: Insights from the 2016 Mw 7.8 Pedernales Ecuador Earth-
929 quake. *Journal of Geophysical Research: Solid Earth*, *125*. Retrieved from
930 <https://onlinelibrary.wiley.com/doi/abs/10.1029/2019JB018001> doi:
931 10.1029/2019JB018001
- 932 Sparkes, R., Tilmann, F., Hovius, N., & Hillier, J. (2010). Subducted seafloor relief
933 stops rupture in South American great earthquakes: Implications for rupture
934 behaviour in the 2010 Maule, Chile earthquake. *Earth and Planetary Science
935 Letters*, *298*(1-2), 89–94. doi: 10.1016/j.epsl.2010.07.029
- 936 Sykes, L. R. (1971). Aftershock zones of great earthquakes, seismicity gaps, and
937 earthquake prediction for Alaska and the Aleutians. *Journal of Geophysical
938 Research*, *76*(32), 8021–8041. doi: 10.1029/jb076i032p08021
- 939 Tassara, A., & Echaurren, A. (2012). Anatomy of the Andean subduction zone:
940 Three-dimensional density model upgraded and compared against global-
941 scale models. *Geophysical Journal International*, *189*(1), 161–168. doi:
942 10.1111/j.1365-246X.2012.05397.x
- 943 Thurber, C. H., & Eberhart-Phillips, D. (1999). Local earthquake tomography with
944 flexible gridding. *Computers and Geosciences*, *25*(7), 809–818. doi: 10.1016/
945 S0098-3004(99)00007-2
- 946 Tilmann, F., Zhang, Y., Moreno, M., Saul, J., Eckelmann, F., Palo, M., ... Dahm,
947 T. (2016). The 2015 Illapel earthquake, central Chile: a type case for a
948 characteristic earthquake ? *Geophysical Research Letters*, *43*, 574–583. doi:
949 10.1002/2015GL066963
- 950 Uchida, N., & Bürgmann, R. (2019). Repeating Earthquakes. *Annual Review
951 of Earth and Planetary Sciences*, *47*(1), 305–332. doi: 10.1146/annurev-earth
952 -053018-060119
- 953 Uchida, N., & Matsuzawa, T. (2013). Pre- and postseismic slow slip surround-
954 ing the 2011 Tohoku-oki earthquake rupture. *Earth and Planetary Science Let-
955 ters*, *374*, 81–91. Retrieved from [http://dx.doi.org/10.1016/j.epsl.2013.
956 .05.021](http://dx.doi.org/10.1016/j.epsl.2013.05.021) doi: 10.1016/j.epsl.2013.05.021
- 957 Universidad de Chile. (2013). *Red Sismologica Nacional. International Federation of
958 Digital Seismograph Networks*. doi: <https://doi.org/10.7914/SN/C1>
- 959 Universidad Nacional de San Juan Argentina. (1958). *West Central Argentina Net-
960 work*.
- 961 Valenzuela-Malebran, C., Cesca, S., Ruiz, S., Passarelli, L., Leyton, F., Hainzl, S.,
962 ... Dahm, T. (2021). Seismicity clusters in Central Chile: investigating the
963

- 964 role of repeating earthquakes and swarms in a subduction region. *Geophysical*
965 *Journal International*, 224, 2028–2043. doi: 10.1093/gji/ggaa562
- 966 van Rijnsingen, E., Funicello, F., Corbi, F., & Lallemand, S. (2019). Rough Subduct-
967 ing Seafloor Reduces Interseismic Coupling and Mega-Earthquake Occurrence:
968 Insights From Analogue Models. *Geophysical Research Letters*, 46(6), 3124–
969 3132. doi: 10.1029/2018GL081272
- 970 Vigny, C., Rudloff, A., Ruegg, J. C., Madariaga, R., Campos, J., & Alvarez, M.
971 (2009). Upper plate deformation measured by GPS in the Coquimbo Gap,
972 Chile. *Physics of the Earth and Planetary Interiors*, 175(1-2), 86–95. doi:
973 10.1016/j.pepi.2008.02.013
- 974 Vigny, C., Socquet, A., Peyrat, S., Ruegg, J. C., Métois, M., Madariaga, R., ...
975 Kendrick, E. (2011). The 2010 Mw 8.8 Maule megathrust earthquake of
976 Central Chile, monitored by GPS. *Science*, 332(6036), 1417–1421. doi:
977 10.1126/science.1204132
- 978 von Huene, R., & Scholl, D. W. (1991). Observations at convergent margins concern-
979 ing sediment subduction, subduction erosion, and the growth of continental
980 crust. *Reviews of Geophysics*, 29(3), 279–316. doi: 10.1029/91RG00969
- 981 Waldhauser, F., & Ellsworth, W. L. (2000). A Double-difference Earthquake lo-
982 cation algorithm: Method and application to the Northern Hayward Fault,
983 California. *Bulletin of the Seismological Society of America*, 90(6), 1353–1368.
984 doi: 10.1785/0120000006
- 985 Wang, K., & Bilek, S. L. (2014). *Invited review paper: Fault creep caused*
986 *by subduction of rough seafloor relief* (Vol. 610). Elsevier B.V. Re-
987 trieved from <http://dx.doi.org/10.1016/j.tecto.2013.11.024> doi:
988 10.1016/j.tecto.2013.11.024
- 989 Wang, K., & Dixon, T. (2004). Coupling semantics and science in earthquake re-
990 search. *Eos*, 85(18), 180. doi: 10.1029/2004EO180005
- 991 Withers, M., Aster, R. C., Young, C., Beiriger, J., Harris, M., Moore, S., & Trujillo,
992 J. (1998). A comparison of select trigger algorithms for automated global
993 seismic phase and event detection. *Bulletin of the Seismological Society of*
994 *America*, 88(1), 95–106.
- 995 Yarce, J., Sheehan, A. F., Nakai, J. S., Schwartz, S. Y., Mochizuki, K., Savage,
996 M. K., ... Todd, E. K. (2019). Seismicity at the Northern Hikurangi Margin,
997 New Zealand, and Investigation of the Potential Spatial and Temporal Rela-
998 tionships With a Shallow Slow Slip Event. *Journal of Geophysical Research:*
999 *Solid Earth*, 124(5), 4751–4766. doi: 10.1029/2018JB017211

1000
1001
1002
1003
1004
1005
1006
1007
1008
1009
1010
1011
1012
1013
1014
1015
1016
1017
1018
1019
1020
1021
1022
1023
1024
1025
1026
1027
1028
1029
1030
1031
1032
1033
1034
1035
1036
1037
1038
1039
1040
1041
1042
1043
1044
1045
1046
1047
1048
1049
1050
1051
1052
1053
1054

Figure 1

Overview map of bathymetry and topography (from the GEBCO 2020 grid; GEBCO_Compilation_Group, 2020) on- and offshore Central Chile. Red-to-white dashed lines are isolines of seafloor age, taken from the model of Müller et al. (2008). Yellow dashed lines offshore mark the two major seafloor features that are subducted along the Central Chile subduction zone, the Challenger Fracture Zone (CFZ - marked by a clear offset of isochrons) and the Juan Fernández Ridge (JFR - visible as a distinct bathymetric high). To the east of the trench, black dashed lines mark depth isolines of the subducting Nazca slab. Colored triangles show the location of seismic stations (network coloring shown in legend) that were used in the present study. The magenta frame shows the extent of the map view projection shown in Figure 3b.

Figure 2

Summary of the presented microseismicity catalog for Central Chile (left) Map view plot of event epicenters, color-coded by hypocentral depth. The solid, barbed red line marks trench location, dashed red lines mark slab surface isodepth contours (40, 80, 120 and 160 km) from the slab2 model (Hayes et al., 2018). The green triangles mark the used seismic stations, the black square marks the location of Santiago de Chile. Blue brackets show the extent of the two profiles in the right subfigure. Yellow dashed lines mark where the seafloor features outlined in Figure 1 impinge onto the study area. The inset in the lower left shows the histogram of local magnitudes for the seismicity catalog. (right) Two east-west profiles of earthquake hypocenters along swaths of 50 km half-width around the latitudes displayed in the bottom left of each subplot. The blue dashed lines mark the slab surface from slab2. The upper panel of each profile plot shows the bathymetry/topography (taken from Etopo1) along its length, averaged over the profile's swath width. Red and blue markers show the location of the trench and the coastline, respectively. In all subfigures, the circles representing earthquake hypocenters are scaled to magnitude as shown in the upper right corner of the left plot.

Figure 3

Plate interface seismicity in Central Chile. a) Historical earthquake rupture length estimates for the years 1700-2000, taken from S. Ruiz and Madariaga (2018). Blue: earthquakes with $M_w > 8.5$, green: earthquakes with $8.5 > M_w > 8$. Slip areas for the two major earthquakes after 2000 are outlined in subfigure b. b) Map view plot of shallow epicenters (hypocentral depths < 60 km) from our catalog; circle sizes are scaled with magnitude. Yellow to blue stars mark the location of repeating earthquake families, their color shows the number of constituent event for each family. Moment tensors for large events after 01/01/2016 (taken from the GEOFON and globalCMT databases) are shown with lower hemisphere beachball projections of their double-couple part, scaled by M_w . The magenta solid line marks the trench location, yellow, orange, red and brown solid lines mark slip contours (2, 5, 10 and 20 m) of the 2015 M_w 8.3 Illapel (northern contours; from Tilmann et al., 2016) and 2010 M_w 8.8 Maule earthquakes (southern contours; from Moreno et al., 2012). The large red star shows the epicenter of the 2017 $M_6.9$ Valparaíso earthquake. Yellow dashed lines west of the trench mark where prominent seafloor features (CFZ - Challenger Fracture Zone; JFR - Juan Fernandez Ridge; see Figure 1) approximately impinge on the study area. Green triangles mark the seismic station network, the black square the city of Santiago de Chile. The latitudinal extent of the three half-ellipse shapes outlined by seismicity are shown in red on the left side of this subplot, their exact outlines are shown in subfigure d). c) Time evolution of catalog seismicity. Yellow stars now mark individual events of a repeater family. Origin times of the 2015 Illapel and the 2017 Valparaíso earthquakes are indicated with red markers. Note that due to sparse network coverage, our catalog is incomplete in the northern part of the study area for the years 2014 and 2015 (Figure 4). d) Plot of seismicity density with the three interpreted half-ellipse shapes outlined by black dashed lines. Earthquake numbers on a grid with $0.05^*0.05$ degree bin size are shown with a logarithmic color scale. For an uninterpreted version of this figure, please refer to Figure S4 in the Supplementary Material.

1055
1056
1057
1058
1059
1060
1061
1062
1063
1064
1065
1066
1067
1068
1069
1070
1071
1072
1073
1074
1075
1076
1077
1078
1079
1080
1081
1082
1083
1084
1085
1086
1087
1088
1089
1090
1091
1092
1093
1094
1095
1096
1097
1098
1099
1100
1101
1102
1103
1104
1105
1106
1107
1108
1109

Figure 4

Station configurations and detected events for the three time periods that make up the presented microseismicity catalog. (left) time period before the 2015 M_W 8.3 Illapel earthquake (29/04/2014 to 15/09/2015); (center) time period between the Illapel earthquake and the 2017 M_W 6.9 Valparaíso earthquake (16/09/2015 to 19/04/2017); (right) time period after the 2017 Valparaíso earthquake (20/04/2017 to 31/12/2018). The blue and red markers at the left side of each subplot show the latitudinal extent of the Illapel and Valparaíso main shocks (from Tilmann et al. (2016) and Nealy et al. (2017)), respectively. Coloring of seismic stations shows the proportion of events for each time period for which this station had P-picks.

Figure 5

Depth evaluation of the hypocenters presented in Figure 3. Left, center and right panels show events with less than 5, less than 10 and more than 10 km vertical distance between event hypocenter and the plate interface as given by the slab2 model (Hayes et al., 2018). Histogram plots at the bottom show the depth distribution of events relative to the plate interface model (negative values mean earthquake occurred above the interface); for each panel the events shown in the top map are highlighted in red.

Figure 6

a) Distribution of GPS measurement sites and grid used for the locking inversions. Blue triangles correspond to GPS sites (refer to the text for a more detailed description of the data sources), red crosses are inversion nodes. b) Results of the unconstrained locking inversion. The distribution of interplate locking is shown, overlain onto the seismicity distribution from Figure 3b, represented by green circles. The arrows represent horizontal GPS observations (blue) and predictions from the shown model (red). Black arrow on the upper left is for scale (20 mm/yr), the achieved overall RMS residual (3.73 mm/yr) is displayed in the bottom right.

Figure 7

Checkerboard resolution test for locking inversion using GPS data. The upper row shows synthetic input patterns of interplate locking, featuring alternating checkers of low (0) and high (0.25, 0.5 and 0.75, as indicated in the top of the different columns) locking degree. The bottom row shows their reconstruction using the same Green's functions and station geometry as for the real data. Note that no noise was superimposed for this test, which implies that the resolution demonstrated here is a best-case estimate.

Figure 8

Constrained inversions of GPS data for interplate locking. a) Definition of three sets of asperities based on the seismicity distribution. b) These asperities are mapped onto the inversion grid for the locking inversion; the red nodes are fixed in the inversions. c) Results of constrained inversion with optimal (i.e lowest BIC; see Figure 9) choice of locking for the fixed nodes of each asperity size. Green dashed lines mark the region of fixed nodes, the locking value those were fixed to is indicated in the upper left of each panel. Blue and red arrows show displacement data and model predictions, respectively. d) Models where locking was fixed to 1 inside the asperity outlines.

Figure 9

a) Comparison between the best-fit constrained model with intermediate-sized asperities (right) and the unconstrained inversion (left). Blue arrows now mark residual GPS vectors (differences between data and model). Black and white contour lines mark locking degrees of 0.7 and 0.9, respectively. Green dashed lines outline the extent of fixed nodes in the constrained inversion. b) Histograms of station residuals in N-S (red) and E-W (blue) direction. c) BIC values for different constrained inversions for different values of fixed locking inside the three different asperity sizes. The horizontal black dashed line represents the BIC for the unconstrained inversion. The six values marked by squares are for the models shown in Figure 8.

Figure 10

Comparison of map view seismicity distributions of events shallower than 60 km between the CSN catalog (left) and the present study (right). Since our catalog is dom-

1110 inated by post-Illapel seismicity, we chose a time period before the Illapel earthquake
1111 (01/2011 - 06/2015) for the CSN catalog here. Note that the seismicity “separators” north
1112 and south of the Illapel rupture (i.e. at about 30.7 and 31.8°S) as well as the aseismic
1113 region roughly corresponding to the main shock rupture (Figure 3) that we found in the
1114 postseismic catalog (right) can already be recognized before the occurrence of the Illapel
1115 mainshock (left). The southernmost such feature offshore Valparaíso is largely absent
1116 in the earlier time period.

Accepted Article

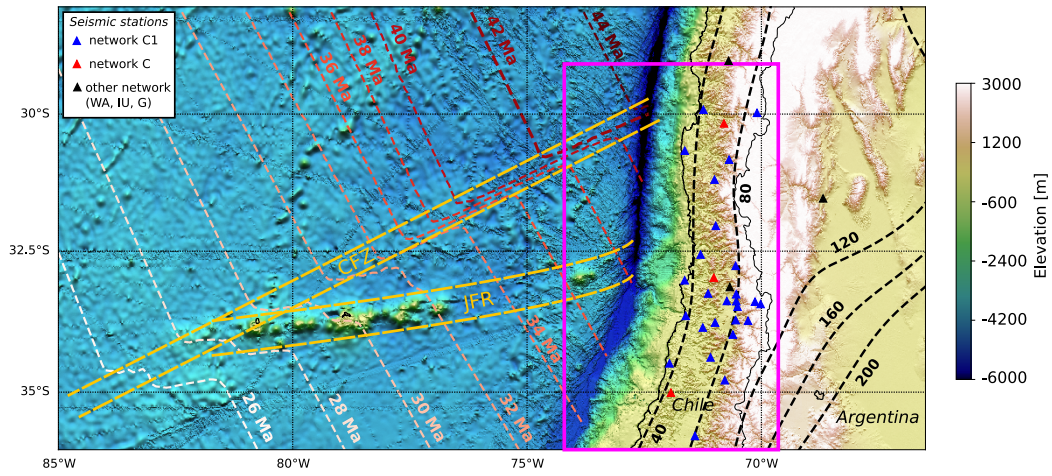


Figure 1.

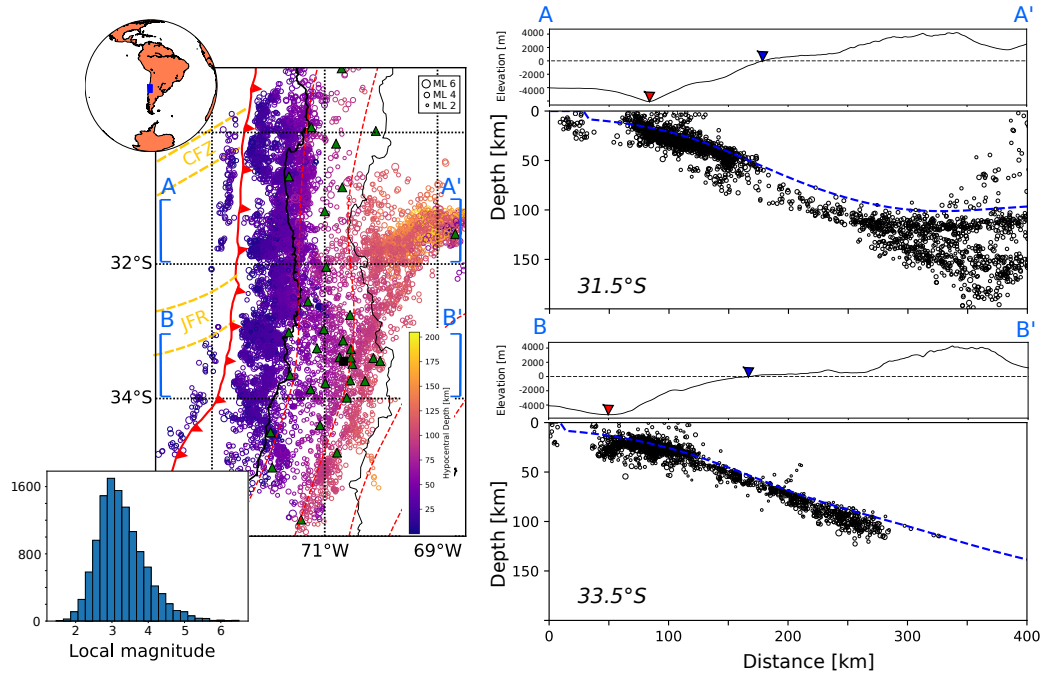


Figure 2.

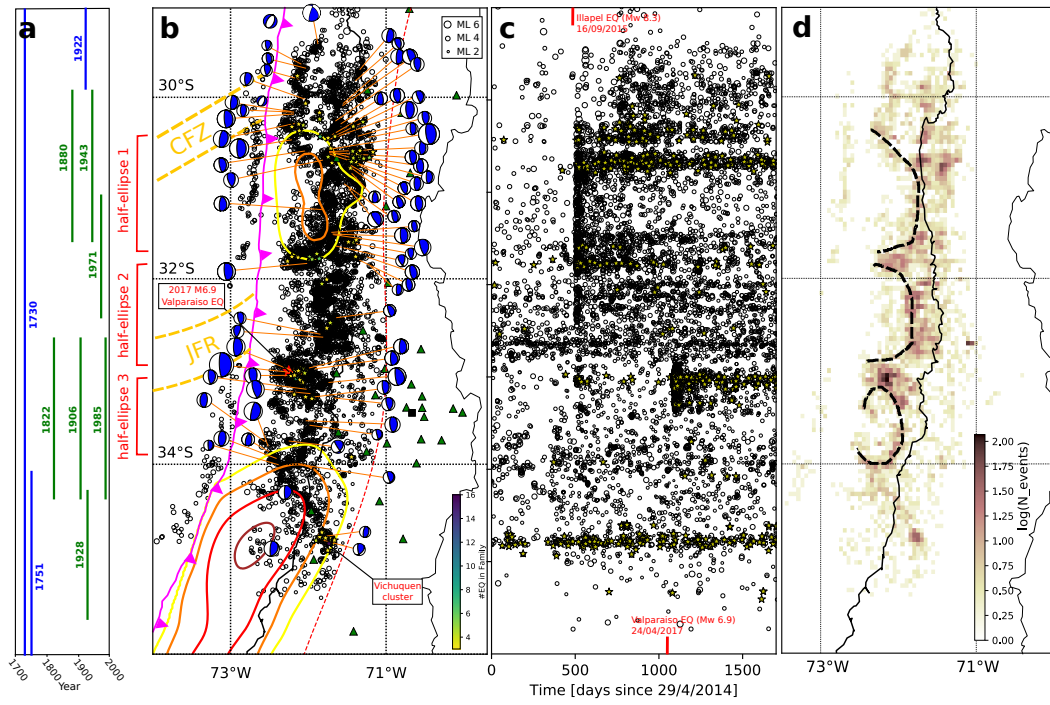


Figure 3.

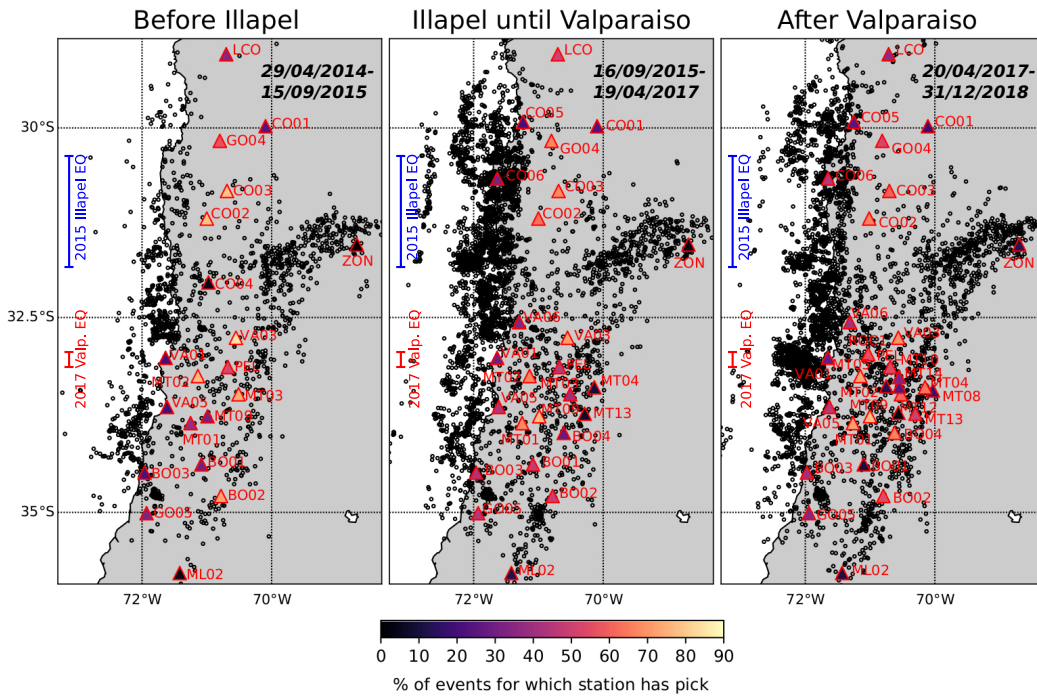


Figure 4.

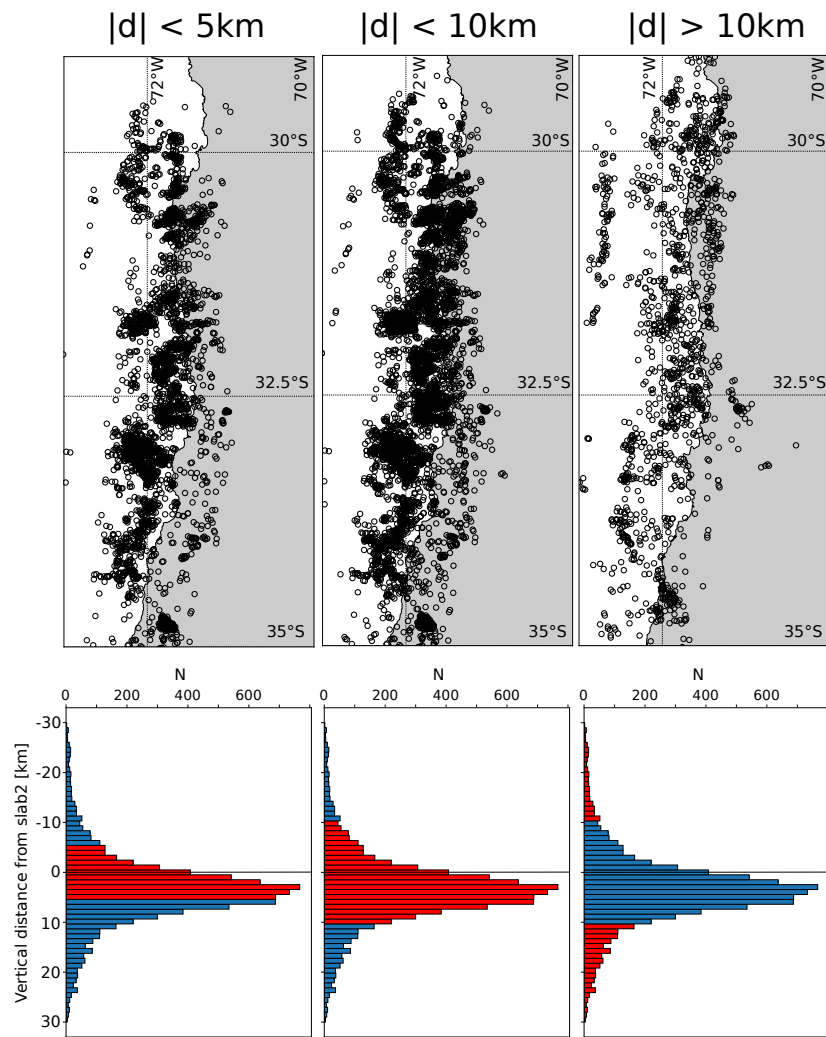


Figure 5.

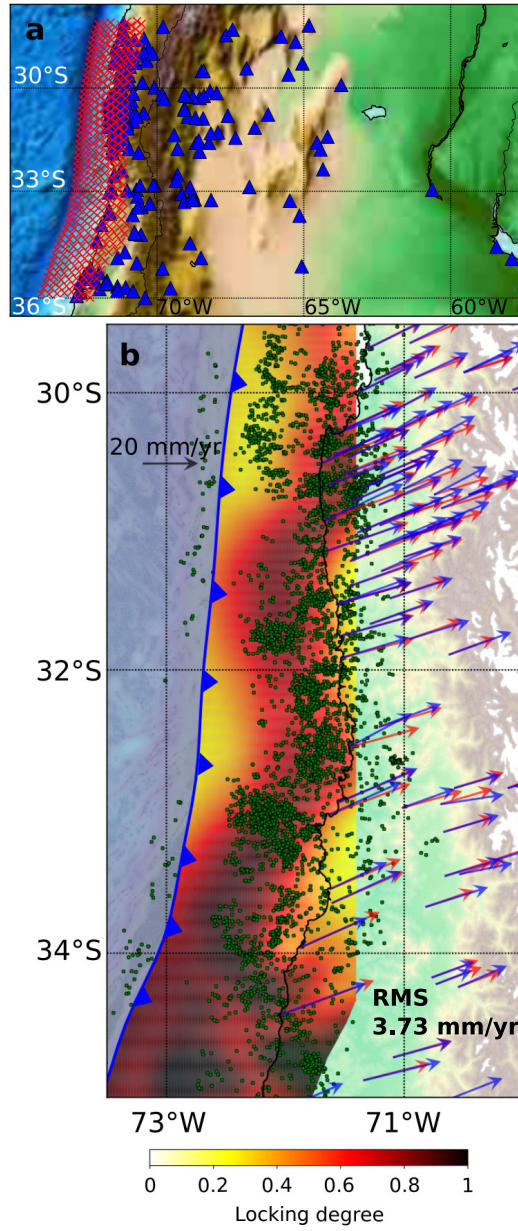


Figure 6.

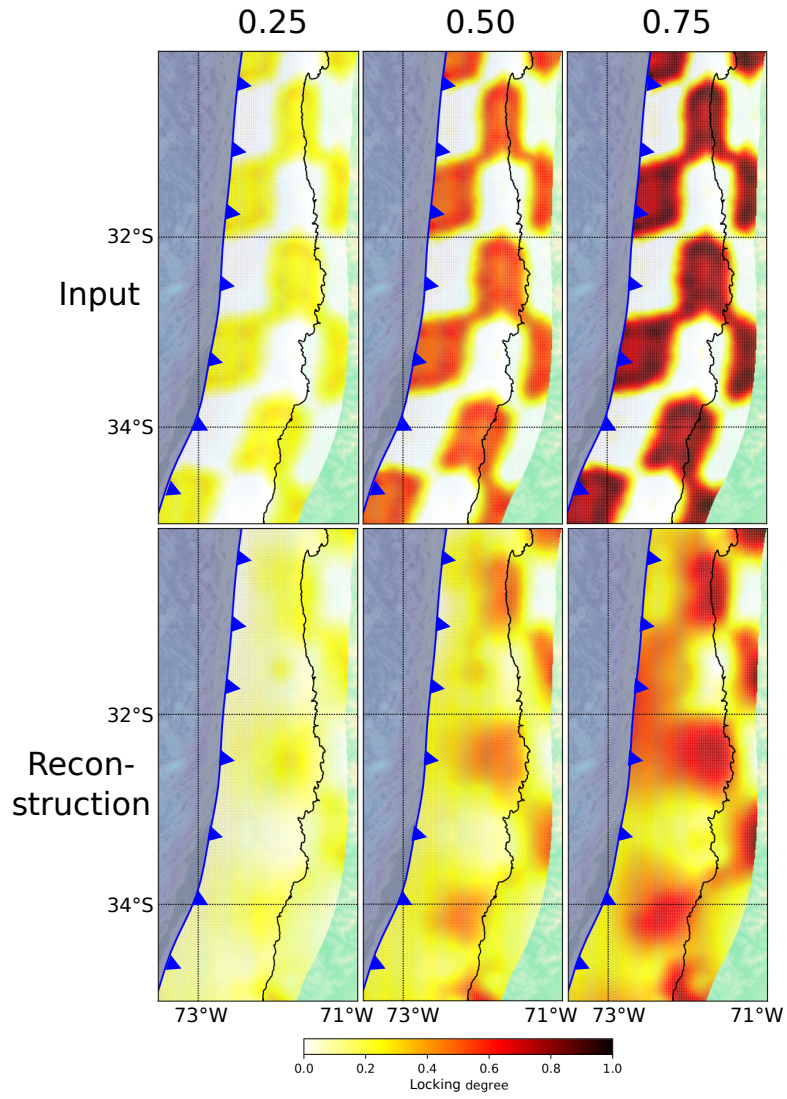


Figure 7.

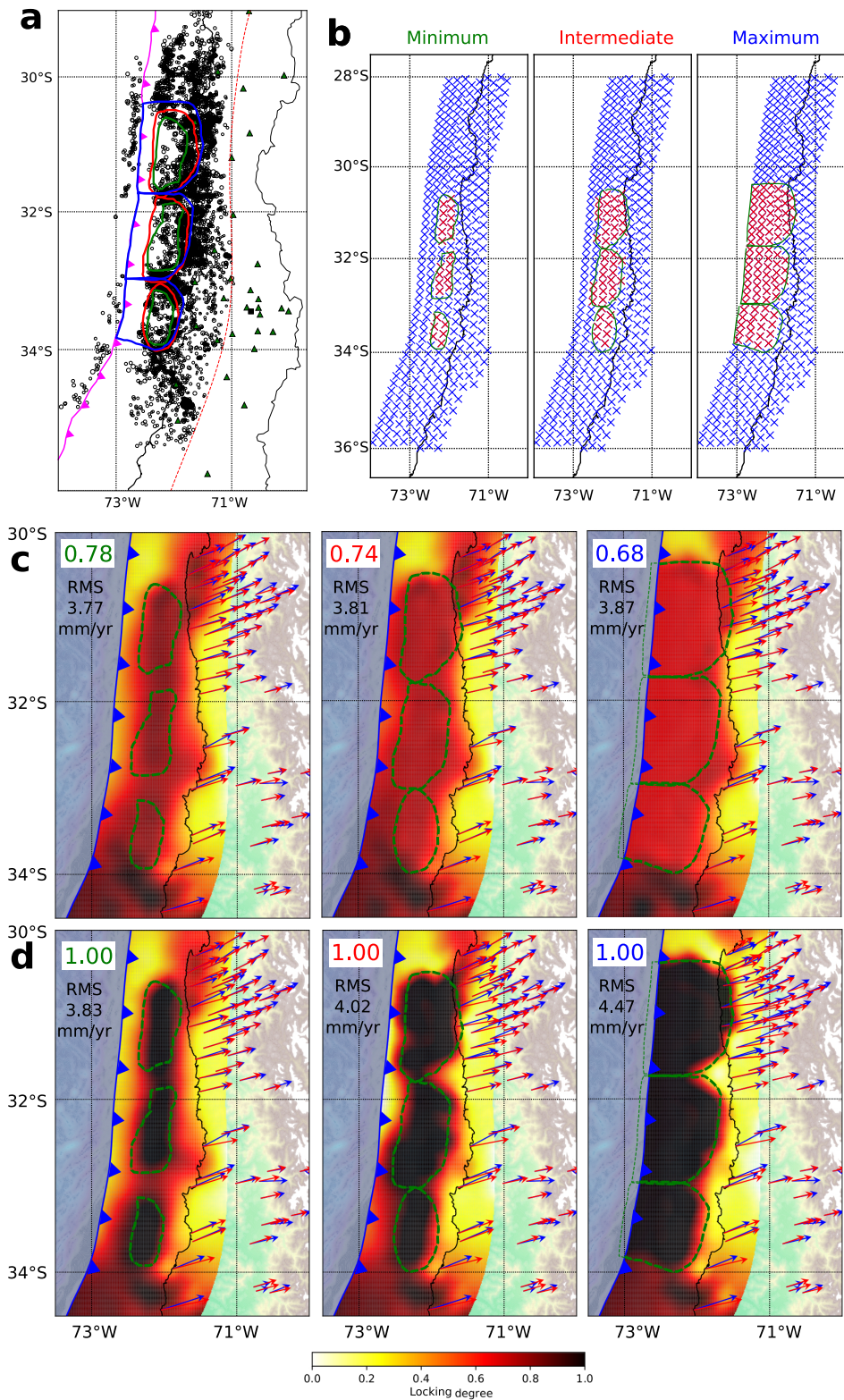


Figure 8.

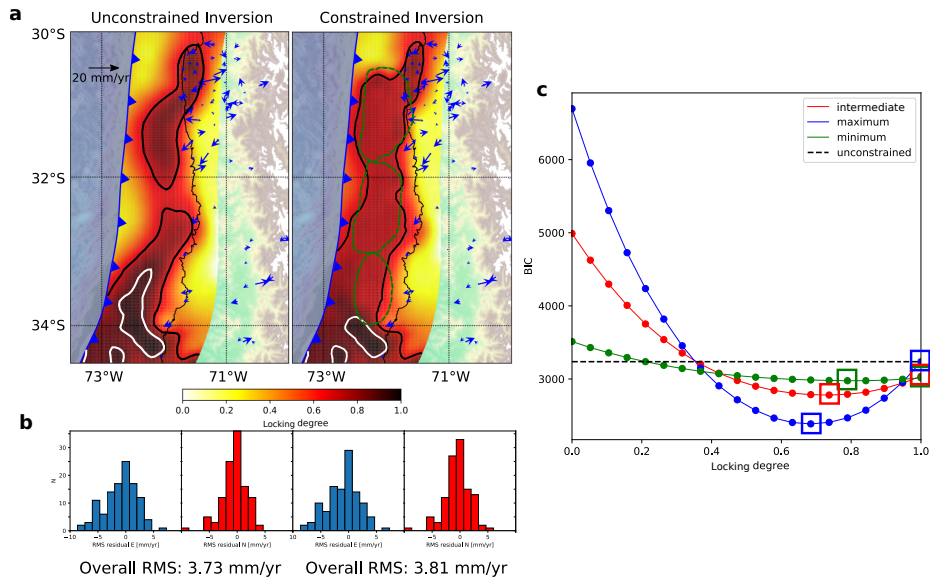


Figure 9.

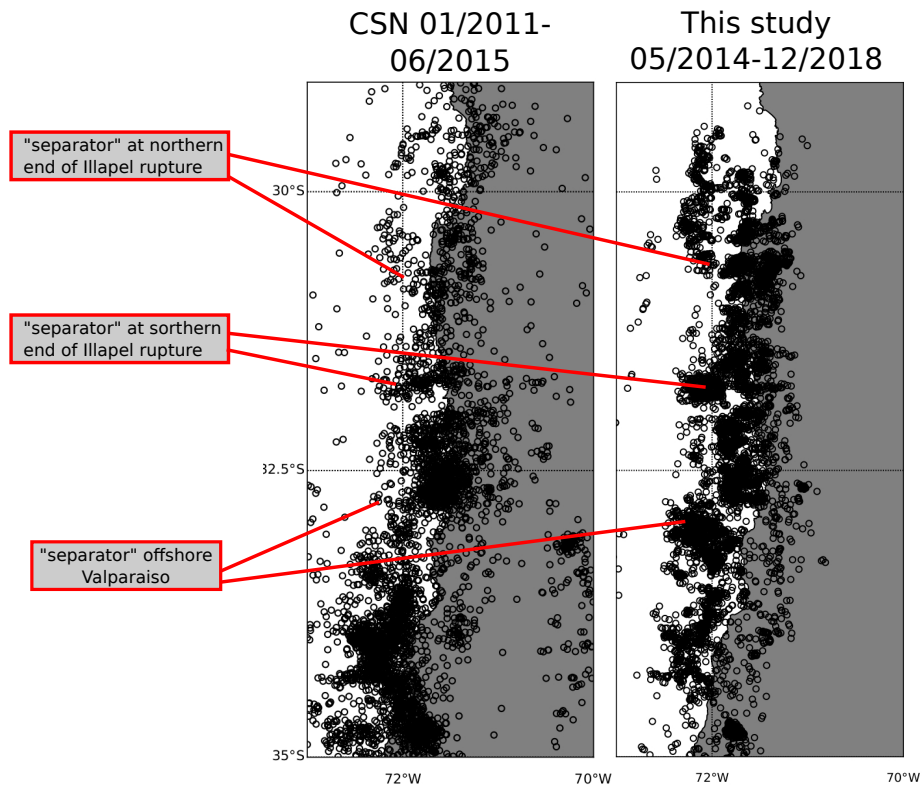


Figure 10.